OSmini: A Microfluidic Platform for Multiplexed, Gradient-Based Drug Delivery on Intact Tumor Slices

Rhutuja Patil

A thesis
submitted in partial fulfillment of the
requirements for the degree of

Master of Science

University of Washington
2025

Committee:
Albert Folch
Ying Zheng

Program Authorized to Offer Degree:
Bioengineering

University of Washington

Abstract

OSmini: A Microfluidic Platform for Multiplexed, Gradient-Based Drug Delivery on Intact Tumor Slices

Rhutuja Patil

Chair of the Supervisory Committee:
Albert Folch
Department of Bioengineering

Traditional preclinical cancer models often fail to predict clinical outcomes, limiting drug development and personalized treatment strategies. Tumor slice cultures offer a physiologically relevant alternative by preserving native tissue architecture and the tumor microenvironment (TME). However, their use has been limited by difficulties in achieving spatially precise drug delivery and ensuring device reproducibility. To overcome these challenges, we developed the OSmini platform—a digitally manufactured microfluidic system for multiplexed, gradient-based drug delivery across intact tumor slices. Using precision CNC milling of poly(methyl methacrylate) (PMMA), we fabricated eight independent microchannels that enable spatially resolved compound delivery with high reproducibility, optical transparency, and chemical compatibility. Flow characterization confirmed uniform performance with less than 8% variability across device iterations. We evaluated lateral diffusion using fluorescein at different flow rates and established operational parameters that maintain spatial precision. Biological validation with fixed and fresh PY8119 murine tumor slices demonstrated successful multiplexed delivery of fluorescent dyes and Doxorubicin gradients. By enabling spatially controlled drug testing in a physiologically relevant *ex vivo* model, OSmini advances functional precision oncology through improved drug screening and tissue-level pharmacodynamic profiling.

Acknowledgements

I would like to express my deepest gratitude to my advisor, Dr. Albert Folch, for his continuous support, guidance, and mentorship throughout my time in the lab. His insight and encouragement have been instrumental in shaping both this project and my growth as a researcher.

I would also like to thank Dr. Lisa Horowitz and Ethan Lockhart for their invaluable contributions to this work and for always being willing to lend a hand. I'm grateful to all the members of the Folch Lab for their support, collaboration, and encouragement at every step of the way.

Finally, I extend my heartfelt appreciation to my parents, whose unconditional support and encouragement sustained me through challenges, and to my friends who provided both moral support and welcomed distractions when needed. Their belief in me has been my foundation throughout this academic journey.

Table of Contents

List of Figures

List of Tables

1. Introduction

Cancer remains one of the leading causes of death worldwide, with approximately 2 million new cases and over 600,000 deaths projected for 2025 in the United States alone [1]. Despite major advances in oncology research and clinical practice over the past decades, including immunotherapies, targeted molecular therapies, and improved surgical techniques, the translation of preclinical drug candidates into effective therapies remains severely limited by poor predictive models [2]. This fundamental challenge in drug development has contributed to the persistently high mortality rates observed across multiple cancer types, particularly in advanced disease states where therapeutic options have become increasingly limited [1].

Traditional preclinical platforms, such as two-dimensional (2D) cell cultures and animal models, which have dominated early-stage drug development for decades, fail to recapitulate human tumor biology, contributing to high failure rates in oncology drug development. The simplistic nature of 2D cell cultures eliminates critical tumor-stromal interactions, three-dimensional architecture, and mechanical forces that significantly influence drug penetration and efficacy [3]. Similarly, while animal models provide an *in vivo* environment, they often poorly reflect human disease progression and treatment response due to fundamental species differences in metabolism, immunity, and tissue architecture [4]. These limitations have directly contributed to the dismal success rates in oncology drug development, with studies indicating that fewer than 4% of oncology drug candidates ultimately receive market approval, compared to approximately 20% across all therapeutic areas [5]. The financial implications are equally concerning, with the average cost to develop a single approved oncology drug exceeding $2.6 billion, largely due to late-stage clinical failures that might have been predicted with more physiologically relevant preclinical models [6].

Functional drug testing using patient-derived tumor tissue has emerged as a promising strategy to mimic native tumor microenvironments and guide personalized therapy [7]. This

approach leverages tumor tissue obtained directly from patients to create testing platforms that maintain the cellular and structural complexity of the original tumor. Various methodologies have been developed, including patient-derived xenografts (PDXs), organoids, and tumor slice cultures, each with distinct advantages and limitations [8]. Among these options, tumor slice culture has gained significant traction within the personalized medicine community due to its ability to preserve native tissue architecture and microenvironmental complexity, making it a physiologically relevant platform for drug response studies. Unlike dissociated models such as organoids or spheroids, tumor slices retain the original spatial organization of malignant cells alongside stromal components, including cancer-associated fibroblasts, tumor-infiltrating lymphocytes, and native extracellular matrix. This preservation of the tumor microenvironment (TME) is particularly crucial given the growing recognition that stromal elements significantly influence treatment response and resistance mechanisms [9].

The application of tumor slice culture for drug testing, however, has been hampered by several technological limitations, including maintenance of tissue viability, standardization of drug delivery, and development of clinically relevant readouts [9]. To address this opportunity, the Folch Lab introduced the Oncoslice platform — a microfluidic solution for personalized cancer drug testing that overcomes longstanding limitations in preclinical screening. This innovative system leveraged principles of microfluidic engineering to enable spatially controlled drug delivery to discrete regions of a tumor slice, allowing parallel testing of multiple compounds on a single tissue sample [10]. Critically, this approach reduced the tissue requirement per drug condition compared to conventional well-based methods, expanding the number of compounds that could be evaluated from limited patient material [11]. However, the original Oncoslice device imposed practical barriers related to fabrication time, reproducibility, and material compatibility with small-molecule drugs. These limitations restricted the broader adoption of the technology for clinical applications and large-scale drug screening initiatives [10], [12].

Despite significant advances in *ex vivo* tumor models, current microfluidic platforms—including earlier systems such as Oncoslice—primarily facilitate discrete, parallel drug delivery without enabling spatial gradients. These approaches fail to replicate clinically relevant conditions in which tumors experience spatially varying drug concentrations, as occurs during systemic chemotherapy, diffusion from the vasculature, or within heterogeneous tumor microenvironments. To address this gap, OSmini was developed as a digitally manufactured microfluidic platform tailored for multiplexed, gradient-based drug delivery to intact tumor slices. Fabricated via precision CNC micro-milling of poly(methyl methacrylate) (PMMA), OSmini offers improved scalability, optical clarity, chemical compatibility, and fabrication reproducibility. The device features eight independent microchannels designed specifically to generate spatial concentration gradients while maintaining uniform flow across tissue samples. This thesis presents the rationale behind the platform, details its design and fabrication, and evaluates its performance through fluidic characterization and biological validation. OSmini thus represents a novel approach to spatially resolved, gradient-based *ex vivo* drug testing, with the potential to enhance personalized cancer therapy and advance preclinical drug development through more physiologically relevant modeling.

1.1 Background – Previous Oncoslice Designs

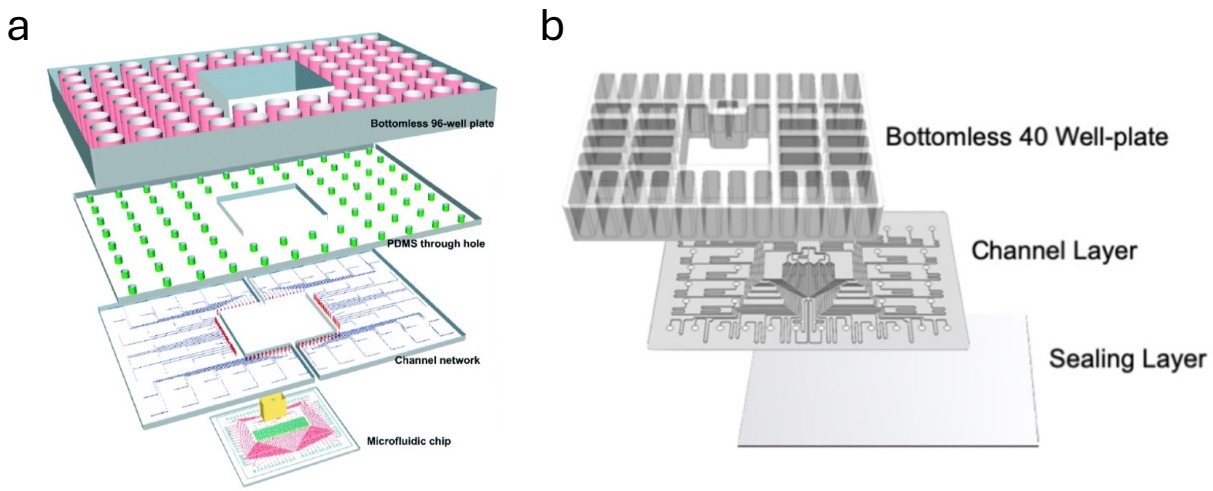

Figure 1. Oncoslice device versions. (a) Layered schematic view of the original Oncoslice device. The device includes (from top to bottom) a modified bottomless 96-well plate, a PDMS layer containing

a through-holes layer, a PDMS microchannel network layer, and the microfluidic chip (where the porous membrane with the tissue is placed). (b) Layered schematic view of the second generation of the Oncoslice device. The device includes (from top to bottom) a modified bottomless 40-well plate, a PMMA channel layer, and a PMMA sealing layer.

The Folch Lab introduced the Oncoslice platform as a novel microfluidic solution for personalized cancer drug testing, aiming to overcome long-standing cancer drug development and preclinical screening limitations. Traditional drug testing paradigms rely heavily on 2D cell cultures and animal models, which often fail to predict human responses accurately because they lack human tumors' structural and biochemical complexity. Dissociated cell systems omit tumor-stromal interactions, vascular and immune components, and extracellular matrix cues, resulting in oversimplified representations of cancer behavior. The high failure rate of oncology drugs in clinical trials—often due to lack of efficacy or safety concerns—highlights the urgent need for physiologically relevant *ex vivo* platforms that preserve the native tumor microenvironment (TME) while enabling multiplexed drug testing.

Chang et al. (2019) developed the first generation of the Oncoslice platform to address this need, which delivered spatially resolved drugs directly onto intact tumor slice cultures (**Fig. 1**a). They fabricated the original platform using conventional soft lithography. They assembled it from a bottomless 96-well polystyrene plate bonded to layered PDMS components. These included a through-hole PDMS layer, a PDMS microchannel network layer, and a thin PDMS chip containing 80 open channels arranged in parallel. The design linked each microchannel to an individual well, allowing the delivery of different drugs or control buffers across the length of the tissue. A porous polytetrafluoroethylene (PTFE) membrane served as a roof to support the tissue slice and seal the open microchannels. Its high permeability, fibrous mesh-like structure, and low surface tension enabled it to form a strong conformal seal with the PDMS substrate—even when moist. The membrane's wicking properties helped maintain tissue hydration and enabled vertical diffusion of fluidic streams from the microchannels directly into the tissue slice in a spatially defined manner. A single syringe pump connected to a common outlet generated flow across all channels,

while variations in microchannel lengths and widths tuned the channel resistances to balance flow rates across the device. This 80-channel system successfully delivered up to 27 unique drug conditions within a single tissue slice, accounting for buffer lanes that reduced lateral diffusion between delivery channels [10].

Although the original Oncoslice device provided a critical proof-of-concept for multiplexed drug delivery to live tissues, several challenges limited its scalability and routine use. The assembly process required high-precision alignment of multiple PDMS layers, often resulting in misalignments, leakage, and device failure. Bonding the PDMS to polystyrene and between PDMS layers required oxygen plasma and silanization, introducing variability and reducing compatibility with certain downstream applications. The fabrication process was labor-intensive and time-consuming, requiring several days to produce a single device through photolithography, mold preparation, PDMS curing, plasma treatment, and final assembly. Furthermore, PDMS's material properties made it suboptimal for drug studies. PDMS tends to absorb and adsorb small molecules, which reduces drug availability and introduces variability in the concentration delivered to tissues. These issues collectively reduced the reproducibility, throughput, and translational potential of the original Oncoslice platform [10].

To overcome these limitations, Rodriguez et al. (2020) developed a second generation of the Oncoslice device using digitally manufactured thermoplastics—specifically poly(methyl methacrylate) (PMMA)—for all structural layers (**Fig. 1**b). They selected PMMA for its biocompatibility, high optical clarity, low gas permeability, and negligible absorption of small molecules compared to PDMS. This version comprised three parts: a bottomless PMMA 40-well plate, a 300 µm-thick PMMA channel network layer containing both closed microchannels and roofless delivery channels, and a 125 µm-thick PMMA sealing layer. The team fabricated all components using CO_2 laser micromachining, enabling rapid prototyping and scalable manufacturing. Unlike the earlier PDMS-based design, the PMMA device required significantly less manual labor. Bonding techniques such as vapor-induced polymer reflow, and thermal pressing provided more consistent sealing. Nevertheless, this

40-channel version presented new challenges. Laser cutting introduced surface roughness and occasional warping of the PMMA layers, which required post-processing steps such as chloroform vapor smoothing and heat-press correction. Additionally, the many channels continued to complicate live imaging and downstream histology [11].

While both the original 80-channel and 40-channel versions aimed to maximize the number of drugs delivered to a single tissue slice, the design motivation behind OSmini diverged significantly. Rather than refining the earlier devices, researchers designed OSmini to meet a distinct experimental need—the ability to perform spatially resolved, short-term drug delivery studies with precise regional control. Unlike its high-throughput predecessors, OSmini targets lower-throughput applications where spatial resolution and gradient control outweigh the need to deliver many drug conditions.

This gradient-based design proves especially useful for several applications: (1) assessing the penetration depth of therapeutic agents across tumor regions with differing vascularity [13]; (2) modeling concentration-dependent immune cell responses at tumor boundaries, where immune infiltration often follows chemokine gradients [14]; and (3) investigating drug resistance mechanisms by exposing tumor regions to varying concentrations of the same compound [15]. The simplified 8-channel design and wider channel spacing offer more precise fluid control, reduce the risk of cross-contamination, and preserve spatial orientation for downstream histological analysis. The smaller footprint and streamlined geometry also improve adaptability for rapid exposure studies, including time-course experiments to monitor dynamic cellular responses.

Although OSmini builds on the foundational concept of spatial drug delivery introduced by earlier Oncoslice devices, it is not a scaled-down iteration, but a purpose-built platform optimized for gradient-based studies in tumor biology and immunotherapy research. The limitations of previous generations and the growing demand for fine-tuned spatial control in tumor microenvironments prompted the development of this specialized platform. OSmini offers a streamlined and precise solution for delivering controlled concentration gradients across intact tumor slices by integrating lessons from earlier designs while serving a

fundamentally different experimental objective. The following section outlines the design principles, fabrication workflow, and technical specifications of OSmini, illustrating how its architecture enables spatially resolved drug delivery with enhanced precision and reduced complexity.

2. Microfluidic Device Overview and Fabrication Protocol

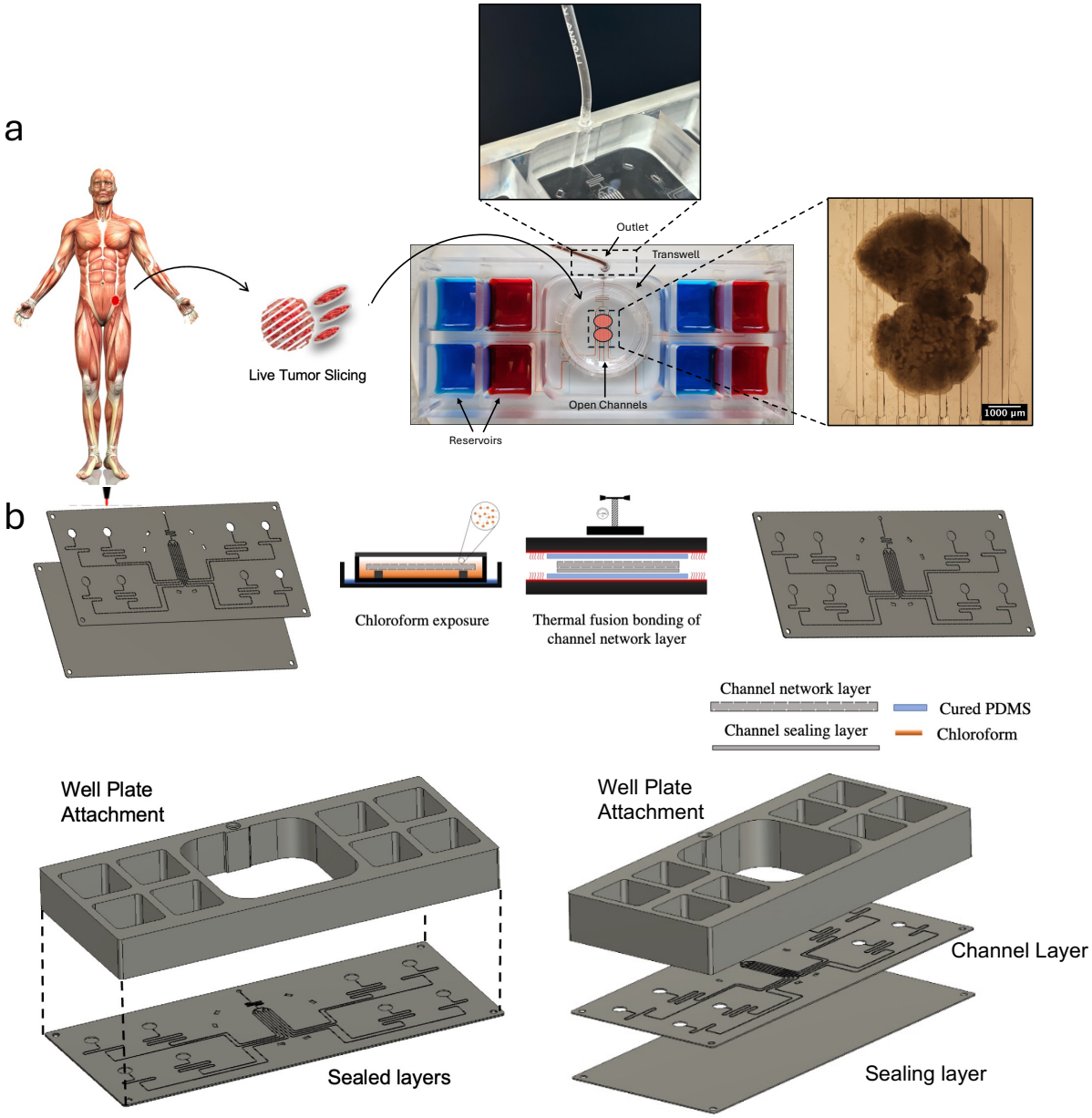

Figure 2. Overview of the OSmini device. (a) Schematic illustration of the experimental workflow and device operation. Live tumor tissue is sectioned and cultured on a porous PTFE membrane, which is then placed over the central open-lane region of the device for spatially resolved drug delivery. The

central image shows the assembled OSmini device loaded with red and blue dyes. Insets show the outlet tubing interface and a tumor slice after treatment. (b) The OSmini platform is composed of three digitally manufactured PMMA layers. Bonding is achieved via chloroform vapor exposure and thermal pressing to create sealed channels, followed by adhesive attachment of the well plate.

Leveraging digital manufacturing, the microfluidic device was designed using 3D CAD software (Autodesk Fusion 360). The design consists of three functional layers: a 12.4 mm-thick PMMA bottomless 8-well plate, a 300 µm-thick PMMA channel network layer, and a 300 µm-thick PMMA sealing layer (**Fig. 2**a). Initial prototypes used a 300 µm channel layer and a 500 µm sealing layer; however, this configuration led to cracking and leakage. The final design utilized a 300 µm channel and 300 µm sealing layer combination, which produced robust, uniform bonds without compromising channel geometry. This platform enables spatially resolved, multiplexed drug testing on intact tumor slices by combining an array of microfluidic delivery channels with a standard-format 8-well plate interface and a single syringe pump-driven outlet.

Tumor slices are cultured on a porous polytetrafluoroethylene (PTFE) membrane, which is placed directly over the open lanes in the device's central culture region. Each well in the top plate acts as a dedicated reservoir feeding into an individual microchannel that converges into an open-lane region in the center culture area, where tissue is placed. These open channels enable the simultaneous delivery of different therapeutic agents, allowing for the simultaneous exposure of a single tissue slice to multiple conditions. All channels converge to a single outlet, where fluid flow is controlled by a syringe pump that pulls liquid at a consistent rate across all lanes, ensuring uniform delivery. A schematic of the tissue workflow and a top-down view of the assembled device during use is shown in **Fig. 2**b, illustrating the spatial layout of the reservoirs, open channels, and central culture area.

The porous membrane serves both as the culture substrate and the functional roof of the delivery channels, effectively sealing the lanes upon contact. This configuration precisely vertically diffuses fluid from each channel into localized regions of the tissue while

maintaining spatial isolation between adjacent lanes. This platform allows live tissue culture and high-throughput delivery of up to eight distinct solutions in a single experiment.

2.1 Digital Fabrication and Device Design

Over the past decade, digital manufacturing has fundamentally reshaped the landscape of microfluidic device development by enabling rapid prototyping, reducing fabrication costs, and improving the reproducibility of device fabrication. Unlike traditional methods that rely on multi-step, labor-intensive processes, digital manufacturing integrates computer-aided design (CAD) and computer-aided manufacturing (CAM) tools with automated fabrication platforms such as CNC (computer numerical control) milling or 3D printing. This approach allows researchers to move seamlessly from a digital design to a functional prototype within hours, greatly accelerating design iteration and enabling scalable production of microfluidic systems with high precision and minimal human intervention [16].

Conventional fabrication approaches, such as photolithography and soft lithography, involve complex workflows that require cleanroom infrastructure, silicon wafer preparation, photomask alignment, PDMS molding, plasma bonding, and manual assembly. These methods are time-consuming, technically demanding, and susceptible to variability between users and batches. In contrast, digital manufacturing—particularly CNC milling—offers a mold-free, mask-free fabrication strategy that directly translates digital files into functional microfluidic devices. As demonstrated by Naderi et al., this enables researchers to prototype new designs in a matter of hours instead of days, allowing for rapid iteration cycles and reducing dependency on specialized infrastructure [16].

The OSmini microfluidic platform was developed using a fully digital workflow that integrated computer-aided design (CAD) and computer-aided manufacturing (CAM) tools within Autodesk Fusion 360. The CAD environment provided micron-level control over critical design parameters, including channel width, depth, inter-channel spacing, and alignment features. Subsequently, the CAM module was used to generate optimized toolpaths and simulate key fabrication parameters such as spindle speed, plunge rate, and

cutting depth. This digital pipeline enabled highly reproducible, geometry-precise fabrication across multiple device iterations, eliminating variability introduced by manual processes and facilitating seamless integration with downstream experimental workflows.

As mentioned before, the device consists of three functional layers: a bottomless 8-well reservoir plate, a channel network layer, and a sealing layer—all fabricated from poly (methyl methacrylate) (PMMA). The enclosed microchannels, which connect each well to the central open lanes, measure 300 μm in depth and 222 μm in width. These dimensions were selected to balance sufficient volumetric throughput with minimal variation in hydraulic resistance, ensuring uniform flow across all channels regardless of their position on the device.

At the center of the platform lies the open delivery region, where each microchannel transitions into a roofless delivery lane. These lanes are 200 μm wide and 550 μm apart (edge-to-edge). This allows for a clear separation between neighboring drug streams and reduces the risk of lateral diffusion between adjacent lanes. The delivery area spans 5.45 mm × 10 mm, a footprint optimized to accommodate up to two tumor slices placed side by side, enabling comparative drug testing within a single run.

The final assembled device measures 115 mm × 50 mm—compact enough to be mounted on most standard inverted or upright microscope stages. Its rigid PMMA construction also improves compatibility with long-term imaging, reduces autofluorescence compared to PDMS, and allows for sterilization using ethanol or UV exposure without warping. This architecture makes this microfluidic platform well-suited for endpoint and live-tissue fluorescence imaging.

Features	**Oncoslice**	**Second-generation**	**OSmini**
Number of Channels	80	40	8

Material/ Microfabrication Technique	PDMS/ Soft lithography	PMMA/ CO_2 laser engraving	PMMA/ CNC Milling
Channel Width/ Spacing	100/150 µm	200/300 µm	200/550 µm
Drug Spacing (edge-edge)	650 µm	850 µm	1300 µm
Reservoir volume	0.4 mL	1.6 mL	3 mL

Table 1. Comparison of microfluidic device design parameters across three generations of Oncoslice platforms.

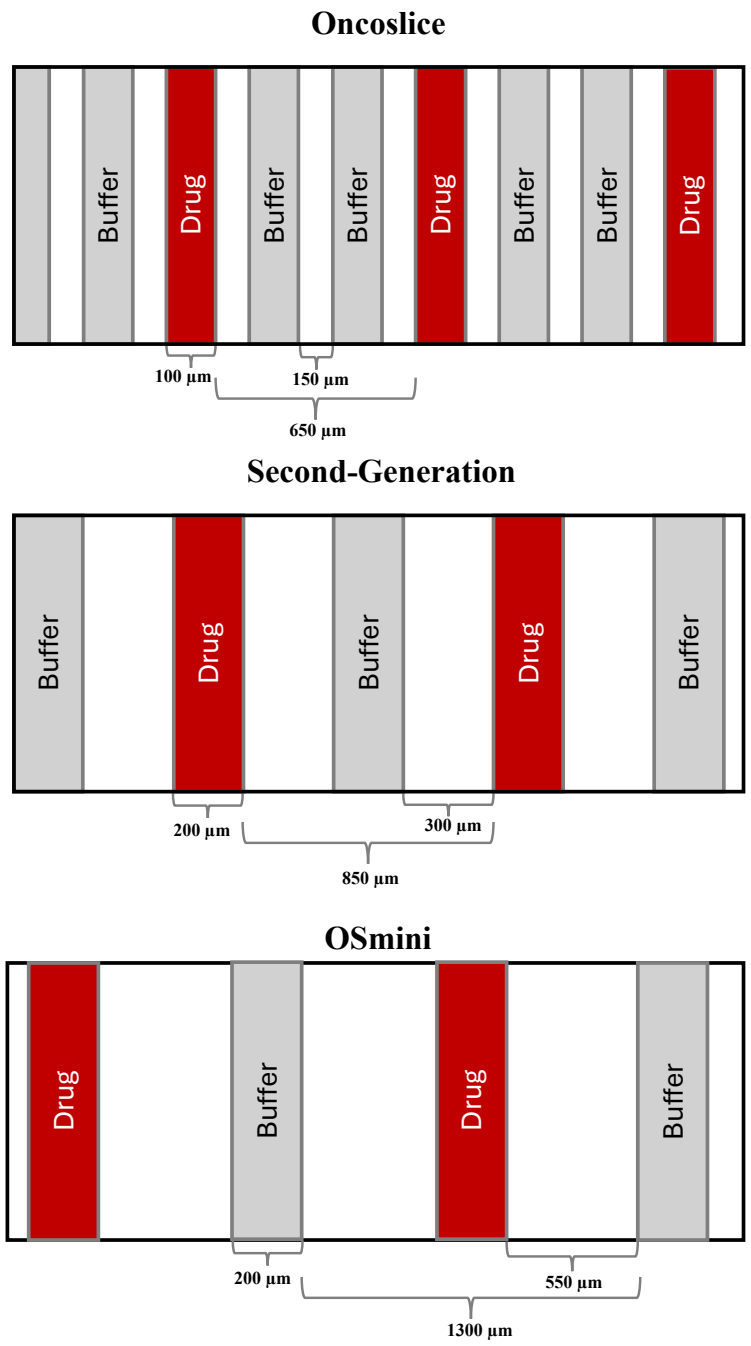

Figure 3. Schematic comparison of channel width, spacing, and drug lane spacing for the open lane region across three generations of the Oncoslice platform. Each layout is shown as a top-down view of the central culture area, where roofless delivery channels (in red) alternate with buffer lanes (in gray) to allow spatially controlled drug delivery to tumor slices.

As shown in **Fig. 3**, the open channels in the original Oncoslice device were designed with a width of 100 µm and a spacing of 150 µm, resulting in a drug lane separation of 650 µm

(edge-to-edge). This high-density layout enabled the delivery of up to 27 different drugs, each flanked by two buffer lanes, within a compact footprint. The 80-channel array included 53 buffer lanes and was designed to alternate drug and buffer streams in a repeated pattern across the width of the tissue. This configuration supported highly multiplexed drug delivery while maintaining spatial separation between treatments using physical buffer zones. Each well in the original system served as an individual reservoir with an approximate volume of 0.4 mL, which can provide up to ~32 hrs of uninterrupted regent delivery at a flow rate of 1 mL/hr.

In the second-generation Oncoslice device, the number of channels was reduced from 80 to 40, allowing for a redesign of the channel architecture. The channel width was increased to 200 µm, and the spacing between lanes expanded to 300 µm, resulting in a drug lane separation of 850 µm. This increase in physical separation between delivery lanes allowed for a more robust spatial organization of treatments and likely contributed to minimizing unintended cross-talk between adjacent streams. By doubling the channel width and increasing spacing, the second-generation platform balanced throughput with improved geometric clarity, enhancing its suitability for precise drug localization experiments. The reservoir volume was also increased to 1.6 mL per well, allowing up to ~64 hrs of uninterrupted regent delivery at a 1 mL/hr flow rate.

Since OSmini was developed to enable controlled spatial variation in drug concentration across a continuous tissue region, the number of channels was reduced from 40 to 8. This reduction increased inter-lane spacing from 300 µm to 550 µm, resulting in a drug lane separation of 1300 µm (edge-to-edge). The wider spacing was essential for minimizing lateral diffusion and enabling the formation of continuous, well-defined concentration gradients across the tissue. This configuration supports experiments focused on dose-response profiling, spatial drug distribution, and localized immune responses. Additionally, the broader lane spacing increases the available area for tissue placement, allowing for testing two tissue slices placed side-by-side. Moreover, the reservoir volume was increased

to also 3 mL, which allowed for ~24 hrs of uninterrupted regent delivery at a flow rate of 1 mL/hr.

2.2 Channel Network and Well Plate Fabrication

The channel network and well plate design were first modeled in Autodesk Fusion 360 using computer-aided design (CAD) and then translated into machine-readable toolpaths via its integrated computer-aided manufacturing (CAM) module. To define milling operations, closed sketch regions corresponding to each microfluidic feature were selected and associated with specific toolpaths, where key parameters such as tool type, spindle speed, feed rate, plunge rate, and cut depth were manually specified for each operation.

All milling was performed on a Datron Neo CNC mill (Datron AG, Germany)—a high-precision, benchtop system capable of spindle speeds up to 40,000 rpm and equipped with an integrated pressure-sensitive probing system for surface mapping. Unlike conventional CNC mills, the Datron Neo enables high-resolution micro-milling with exceptionally fine tools (as small as 0.1 mm in diameter) and allows real-time Z-height compensation based on surface topology. These capabilities were critical for reliably fabricating shallow microfluidic features in PMMA, especially given the material's inherent thickness variability. The system's compact footprint and advanced automation features made it well-suited for rapid prototyping and reproducible device fabrication in a laboratory setting.

The toolpaths were organized by feature type—creating separate operations for enclosed channels, open delivery lanes, outlet ports, and the exterior chip profile. This feature-based modularization allowed greater control over tool selection and milling depth, especially when switching between features requiring different endmills or depth tolerances.

Layer	Surface Profile points (#)	Features	Tool Diameter (mm)	Spindle Speed (rpm)	Feed Rate (mm/min)
	400	Open channels	0.149	33k	265

Microchannel Layer		Enclosed Channels	0.149	33k	265
		Inlet and outlet holes	0.793	25k	1500
		Transwell Feet	0.3048	33k	535
		Layer contour	0.381	25k	800
Well Plate	300	Wells	3.175	12.5k	2500
		Outlet Pocket	1.5875	25k	2100
		Outlet hole	0.793	25k	1500
		Well plate contour	3.175	12.5k	2500

Table 2. CNC milling parameters for the channel layer and well plate.

To accommodate the varying geometries and depths of the microchannel and well plate layers, milling operations were separated by feature type and assigned to specific endmills, spindle speeds, and feed rates, as outlined in Table 2. Small diameter endmills were used for precise channel features, while larger tools were reserved for wells and contours to increase throughput. This structured, feature-specific approach to toolpath generation and milling parameter selection improved fabrication consistency and allowed for precise control over both fine and large-scale device features.

Achieving consistent milling depth across the device surface also required accounting for topographical variation in PMMA stock. PMMA stock sheets used for milling are subject to thickness variation due to the manufacturing process. PMMA is commonly cell-cast between two glass plates, which can sag or bow, leading to topographical irregularities across the sheet's surface. The thickness variation that was observed was of ± 10-20%. This variability posed a significant challenge when attempting to mill shallow features such as the enclosed channels, as inconsistent contact between the tool and surface could result in undercut or missed cuts altogether.

To address the variability in the PMMA substrate thickness, the "surface profile" function of the Datron Neo CNC mill was utilized. This feature employs a pressure-sensitive probe to measure the surface height at evenly spaced calibration points across a defined milling

area. These measurements are then used to generate a 3D surface map, allowing real-time spindle height compensation during the milling process. By increasing the number of calibration points, the machine can more accurately track surface undulations, though at the expense of processing time. This compensation ensured consistent milling depth across the entire device surface, enabling reliable fabrication of fine features.

2.3 Post-ablation Process

Following CNC milling, a series of washing and cleaning steps were required to remove residual PMMA debris, microplastic particles, and burrs generated during the milling process. These contaminants can obstruct microchannels, interfere with bonding between layers, or compromise optical quality during imaging if not adequately removed. The channel layer was cleaned using a mild detergent solution and water to remove loose particulate matter and machining oil residues. The layer was gently scrubbed using a soft brush to dislodge debris from narrow features such as the enclosed channels. After rinsing thoroughly with water, the layer was dried using an air gun.

To further clear out any residual burrs or debris lodged within the carved microchannels, a fine metal pick was used to trace along the channel paths under a stereomicroscope manually. This step was beneficial for removing larger fragments or edge burrs that resisted brushing or rinsing. A dry toothbrush was used to perform a secondary cleaning pass. The brush was angled to ensure the bristles could reach into channels and through holes, removing any residual material without damaging the channel walls. An additional round of soap washing, water rinsing, and pressurized air drying was performed to remove the remaining debris. The 8-well plate was also cleaned using a mild detergent and water rinse, followed by air drying with a pressurized air gun to eliminate trapped moisture from the milled wells and outlet pockets. All the cleaned layers were stored in a clean, covered container to prevent contamination prior to bonding.

2.4 Bonding and Assembly Protocol

One of the most important aspects behind the performance and reliability of a microfluidic device is the bonding process, as it determines fluidic sealing, channel fidelity, and overall

device functionality. Following fabrication, the OSmini device was assembled using a sequential bonding strategy to achieve fluidic sealing and mechanical integration across the three-layer PMMA structure. As shown in **Fig. 2**b, the assembly consisted of two bonding stages: (1) thermal solvent bonding to enclose the microchannels and (2) adhesive bonding to integrate the sealed microchannel assembly with the milled well plate.

The microchannel and sealing layers were bonded using a chloroform vapor-assisted thermal bonding process to achieve reliable, adhesive-free sealing of PMMA microfluidic components. This method softens the bonding surfaces through solvent vapor exposure, promoting polymer chain entanglement at the interface. One of the significant advantages of chloroform vapor bonding is its ability to produce strong, cohesive bonds while preserving delicate microchannel geometries, as it operates at temperatures significantly below the glass transition temperature of PMMA, thereby reducing the risk of deformation or collapse. Furthermore, because it forms a direct PMMA–PMMA interface without any intermediate adhesive layer, this technique produces high optical clarity, making it especially suitable for fluorescence imaging applications. Compared to traditional liquid solvent bonding or thermal fusion, vapor-phase bonding offers improved control over solvent exposure, reducing the likelihood of channel over-etching or material warping [17].

Based on bonding protocols previously established for earlier generations of the Oncoslice platform, a similar chloroform vapor-assisted thermal bonding approach was adopted for OSmini, as described below. A glass container (11-cup Pyrex dish) was prepared as the vapor chamber by placing eight stainless steel standoffs (3 mm height) at the bottom to elevate the PMMA layers. 50 mL of chloroform was poured into the chamber and allowed to equilibrate for 5 min, with the lid partially covered to saturate the vapor environment.

During this period, the microchannel layer was cleaned using an air gun to remove any surface dust or lint and then kept protected under a clean stainless steel container lid. After vapor saturation, the 300 µm-thick channel layer and the sealing layer were placed face-down on the elevated standoffs inside the chamber — with the engraved side of the microchannel layer oriented downward. The layers were exposed to chloroform vapor for 4

min under a partially sealed environment. Immediately after exposure, both layers were removed and quickly aligned with their solvent-softened faces pressed together. Manual pressure was applied to each corner using fingertips while intentionally avoiding the central open channel region to prevent feature distortion. This initial hand pressing helped establish conformal contact at the edges and fixed alignment before thermal bonding.

The sealed microchannel and sealing layer assembly were sandwiched between two three mm-thick PDMS pads to ensure uniform pressure distribution. The padded stack was placed between flat aluminum plates and inserted into a manual heat press (Carver Model 4386). The bonding was carried out at 140 °F under 240 psi for 6 min. These conditions were selected to maintain the softened polymer state induced by chloroform vapor exposure while avoiding the deformation of the microchannel structures. The mild thermal pressure facilitated polymer chain entanglement, resulting in a robust, irreversible fusion bond. After pressing, the device was allowed to cool at room temperature to stabilize the bond and minimize the risk of delamination due to thermal contraction.

Once the microchannel and sealing layers were permanently bonded, the resulting two-layer assembly was aligned and bonded to the milled 8-well plate to complete the device structure. Before the well plate was bonded to the microchannel assembly, alignment and outlet holes were finalized to enable tubing integration and ensure accurate registration of all device layers. Although the CAD model included through-holes for these features, the CNC mill could only create shallow pilot holes during milling due to the PMMA plate's thickness exceeding the cutting tool's length. As a result, the holes were not thoroughly drilled through and required manual post-processing. The outlet and alignment holes were manually drilled using the shallow CNC-milled recesses as guides using a WEN 5-speed drill press (Model 4208, 8-inch, 1/3 HP motor). The outlet port — positioned centrally at the base of the plate — was drilled using a 2.286 mm Ø × 15 mm drill bit to match the dimensions of a 2.44mm SILGARD® tubing and enable a snug, press-fit seal. Additionally, four alignment holes were drilled at the corners of the well plate using a 2.032 mm Ø × 13.5 mm drill bit to match the pre-cut holes in the channel and sealing layers.

Ensuring robust adhesion between the microchannel assembly and the well plate was critical to maintaining fluidic isolation and structural alignment across all channels and wells. A 50 µm-thick pressure-sensitive adhesive (300LSE High-Strength Acrylic PSA, 3M™, USA) was used as an interfacial layer. The outline of the well plate, including cutouts for the wells, outlet ports, and alignment holes, was directly derived from the original CAD design to ensure exact registration. This design was exported in vector format to laser-cut the pressure-sensitive adhesive using a CO_2 laser system (VLS3.60, Universal Laser Systems, Scottsdale, USA). The laser parameters were optimized to ensure clean edges and dimensional precision. Once cut, the adhesive sheet was carefully transferred to the bottom of the sealed microchannel assembly using a pair of tweezers and alignment pins to ensure proper registration. After adhesive placement, the assembly was aligned to the well plate using the same guide holes, ensuring that the inlet wells and outlet ports were precisely matched. To secure the bond, manual pressure was applied uniformly across the surface using fingertips, focusing primarily on the perimeter and around the well cutouts to ensure complete adhesive contact. This approach was sufficient to establish a robust seal between the layers.

Following the device assembly, outlet tubing was inserted into the outlet port located at the top of the milled well plate to facilitate fluid extraction. A 2.44 mm OD SILGARD® tubing (Dow Corning, USA) was used for its flexibility, chemical resistance, and compatibility with biological media. The tubing was inserted into the outlet hole, and the pocket around the outlet was filled with Gorilla Superglue to ensure a complete seal and hold the tubing in place. This approach resulted in a robust, airtight outlet connection, supporting consistent device operation and ease of handling during experiments. After insertion, the tubing was left undisturbed overnight, allowing the adhesive (Gorilla Superglue) to cure and ensure long-term sealing integrity. Additionally, the use of optically clear PMMA allowed real-time visual monitoring of fluid flow throughout the device. As a final preparation step before biological experiments, the fully assembled device was exposed to oxygen plasma treatment for 5 min to sterilize the internal surfaces and enhance the hydrophilicity, promoting uniform fluid filling and minimizing bubble formation during flow.

2.5 Fabrication Time

Step	Time (mins)
CNC Milling	
Microchannel Layer	80
Well Plate	35
Sealing Layer	0.2
Post-ablation Process	
Microchannel Layer	15
Well Plate	3
Assembly	
Microchannel layer to sealing layer bonding	16
Well plate to microchannel layer bonding	10
Outlet insertion	3
Total time	**162.2**

Table 3. Total device Fabrication Time.

The total time required to fabricate a single OSmini device is approximately 162 min, as outlined in Table 3. The fabrication includes CNC milling, post-ablation cleaning, layer bonding, and final outlet insertion. Notably, the microchannel layer milling step alone accounts for nearly 50% of the total fabrication time (80 min), primarily due to the large surface area of the design, which increases toolpath complexity and prolongs cutting duration. Despite this, the overall fabrication time reflects a substantial improvement in

manufacturing efficiency. The simplicity and accessibility of the protocol reduce fabrication costs and enable users with minimal microfabrication experience to reliably reproduce the device. Multiple OSmini units can be fabricated within a single day and prepared for experimental use the following day, making this workflow highly suited for rapid prototyping and small-batch production.

3. Device Challenges and Troubleshooting

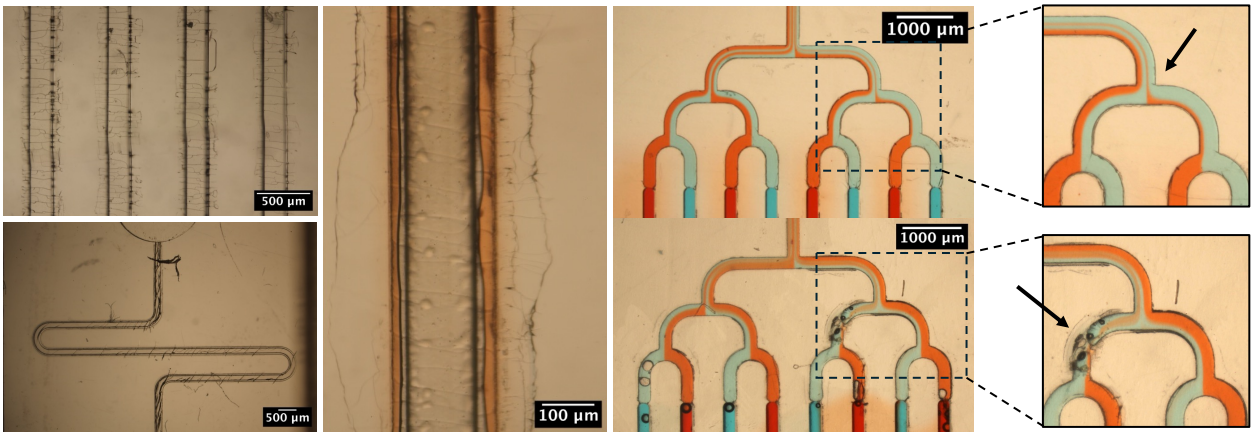

Figure 4. Device operational issues. Schematics illustrate recurring microfluidic device issues, including microcracks, restricted flow, and seal degradation at channel interfaces. Zoomed-in views highlight regions of flow disruption caused by surface irregularities, bonding defects, or partial blockages within the channel network.

Early device prototypes using a 500 µm-thick PMMA sealing layer exhibited several recurring operational issues that emerged during testing and repeated use. Microscope images in **Fig. 4** document these challenges, which primarily affected channel integrity, bonding performance, and fluid delivery reliability. One of the earliest signs of suboptimal device behavior was difficulty achieving clear, high-resolution fluorescence imaging. Despite successful channel fabrication and bonding, images captured through the 500 µm sealing layer consistently appeared blurry or lacked sharp contrast. The increased optical path length and refractive distortion introduced by the thicker PMMA contributed to reduced image clarity, especially when imaging.

In addition to imaging challenges, mechanical and fluidic issues became apparent during routine operations. The most prominent issue was the formation of microcracks at or near the channel interfaces. These cracks likely arose from uneven stress distribution during thermal bonding or from mechanical strain over time. The thickness of the sealing layer made it more rigid and less conformal, reducing its ability to adapt to subtle surface variations during bonding. As a result, localized gaps or stress concentrations formed, especially in areas with small-radius curves or at transitions between open and enclosed regions. Seal degradation was another frequent observation. In several devices, bonding appeared initially successful but progressively failed after extended use, leading to delamination at the interface. This compromised the fluidic seal and enabled leakage into adjacent regions. Flow irregularities were also typical. Some channels exhibited significantly reduced or asymmetric flow despite having identical designs. These disruptions were caused by partial blockage from debris or incomplete channel sealing. In a few cases, the bonding interface formed shallow gaps that narrowed or collapsed sections of the channels, disrupting laminar flow and altering delivery patterns.

To address these limitations, sealing layers of varying thicknesses were systematically tested. The 300 μm-thick PMMA sealing layer consistently demonstrated the most reliable performance. Compared to thicker alternatives, the 300 μm layer improved imaging clarity and produced more uniform bonding during assembly. This optimization significantly reduced the occurrence of delamination, microcracking, and flow irregularities, thereby enhancing the device's overall structural integrity and operational consistency.

3.1 Enhanced Surface Profiling for Uniform Channel Depth

Achieving uniform channel depth is critical for the performance of microfluidic devices, as variations in depth can impact fluid resistance, flow uniformity, and bonding integrity. One of the key challenges encountered during the CNC milling of PMMA sheets was the inherent thickness variability. These sheets often exhibit topographical fluctuations of ±10–20% of the nominal thickness, which is especially problematic when machining shallow features such as microchannels.

Initially, the number of points was set between 300 and 400, which provided only a coarse approximation of the surface profile. This level of resolution was insufficient to compensate for height differences across large-format designs like the OSmini channel layer, resulting in inconsistent cut depths and partial or failed channel milling.

To address this, the number of surface profiling points was increased to 900–950 in later iterations of the fabrication workflow. This higher density of measurement points enabled the machine to generate a more detailed and accurate 3D surface map. This enhancement significantly reduced the incidence of depth-related fabrication defects such as undercuts, burr formation, and channel edge irregularities. It also improved feature fidelity across the device footprint, ensuring consistent fluidic resistance. By enhancing the precision of microchannel milling, this modification contributed to higher device reproducibility and reduced post-fabrication troubleshooting and rework.

3.2 125 µm Thick Sealing Layer

Protocol	*Chloroform Exposure (mins)*	*Heat Press Temp (°F)*	*Pressure (psi)*	*Press Time (mins)*
A	Channel layer: 3 Sealing layer: 3.5	120	200	6
B	Channel layer: 3 Sealing layer: 3.5	120	80	8
C	Channel layer: 4 Sealing layer: 4	140	240	4

Table 4. Various bonding protocols tested with 125 µm sealing layer.

To determine the most effective bonding conditions, a 125 µm-thick PMMA sealing layer was used—primarily because it was the thinnest stock available during fabrication. This thickness allowed the evaluation of how well the layers bond when using a thin material and to observe how reduced stiffness might affect the quality of the seal. A variety of bonding protocols were tested, as shown in Table 4. Each protocol systematically varied key

parameters, including chloroform vapor exposure times, thermal press temperature, applied pressure, and bonding duration, to evaluate their effects on sealing performance.

Initially, a bonding protocol similar to that used for thicker sealing layers was selected as the baseline. In this method, the microchannel and sealing layers were individually exposed to chloroform vapor—3 min for the channel layer, followed by 3.5 min for the sealing layer. During the exposure of the sealing layer, the microchannel layer was kept covered under a metal container lid to minimize dust contamination and solvent evaporation. Once exposed, the two layers were aligned and bonded using a heat press at 120 °F under 200 psi for 6 min. However, upon removal from the press, the layers exhibited cracking and warping along the bonded interface. The combination of high pressure and prolonged heating exceeded the mechanical tolerance of the thinner PMMA, resulting in a brittle fracture. To mitigate this, subsequent trials adjusted the bonding parameters by lowering the pressure.

In the second bonding trial, the same chloroform vapor exposure times were maintained—3 min for the channel layer and 3.5 min for the sealing layer—as in the previous attempt. However, to address the cracking, the bonding pressure was significantly reduced to 80 psi, and the press time was extended to 8 min while keeping the temperature constant at 120 °F, hoping this adjustment would reduce the mechanical stress. The bonded layers showed no cracks after removal from the heat press. However, there were a lot of air pockets across the bonded interface. Additionally, many of the microchannels were visibly unsealed, particularly along the central regions of the layer. This outcome demonstrated that although the reduced pressure mitigated mechanical damage, it did not ensure a robust fluidic seal across the device.

The bonding parameters were further modified in the third attempt to enhance sealing reliability while minimizing mechanical stress. The channel and sealing layers were exposed to chloroform vapor for 4 min, slightly longer than in previous trials, to promote more complete surface softening. Bonding was performed at an elevated temperature of 140 °F under 240 psi for a shorter duration of 4 min. This combination was selected to provide sufficient thermal energy and contact pressure within a shorter time frame to prevent

overheating or distortion of the thin 125 µm sealing layer. Upon initial inspection, the bonded device exhibited only minor air bubble formation. Importantly, fluid flow was observed through the channels following oxygen plasma treatment, indicating functional channel connectivity and sufficient bonding for fluidic operation. However, small surface cracks began appearing around the bonded interface after several hours. These cracks likely resulted from residual thermal or mechanical stress imposed during pressing, exacerbated by the reduced mechanical robustness of the thinner sealing layer.

In contrast, this protocol progressed toward a usable seal; the emergence of cracking highlighted the need for further adjustment to balance bonding strength with material durability. However, during subsequent flow rate experiments, the device began to crack near the bonded interface. These failures emphasized the limitations of applying high mechanical force to low-thickness substrates. They highlighted the need for further protocol refinement to achieve durable bonding without compromising the structural integrity of the device during operation.

3.3 300 µm Thick Sealing Layer

Protocol	*Chloroform Exposure (mins)*	*Heat Press Temp (°F)*	*Pressure (psi)*	*Press Time (mins)*
A	Channel layer: 3 Sealing layer: 3.5	140	200	5 min + rotate 90°, flip 180°, 2 min
B	Channel layer: 4 Sealing layer: 4	140	240	6

Table 5. Various bonding protocols tested with 300 µm sealing layer.

Given the limitations encountered with the 125 µm sealing layer, subsequent bonding experiments were conducted using a 300 µm-thick PMMA sealing layer. This thickness offered increased mechanical stability while remaining compatible with high-resolution microfluidic features, allowing for a more robust evaluation of bonding conditions under similar fabrication workflows. In the first protocol, the microchannel layer was exposed to

chloroform vapor for 3 min and the sealing layer for 3.5 min, following which the layers were aligned and heat pressed at 140 °F and 200 psi. To ensure even bonding, the assembly was pressed for 5 min, rotated 90°, flipped 180°, and pressed again for two additional min. Initially, the layers appeared well bonded and properly aligned, with no visible cracks or delamination. However, during fluidic testing, a few channels exhibited uneven flow behavior, and after 2–3 uses, one of the channels began to pull in air. This suggested the presence of a micro gap or a weakened seal, likely due to incomplete bonding at specific channel interfaces. While the overall bonding held structurally, the fluidic inconsistency required further refinement in pressure distribution and interface contact during bonding.

In the second trial, the microchannel and sealing layers were simultaneously exposed to chloroform vapor for 4 min in the same container, streamlining the vapor exposure step. After exposure, the layers were quickly aligned and pressed at 140 °F under 240 psi for 6 min. This protocol aimed to increase bonding strength by maximizing solvent activation and applying higher pressure. The bonded layers appeared visually clean and well-aligned upon inspection, with minimal visible defects or bubbles. During flow testing, channels demonstrated consistent flow without signs of leakage or delamination. This protocol demonstrated excellent reproducibility and was ultimately adopted as the final bonding strategy due to its reliable performance and ease of execution. Together, these bonding trials established an optimized protocol using a 300 µm sealing layer and simultaneous chloroform exposure, which consistently yielded structurally stable devices with reliable fluidic performance and minimal fabrication defects.

4. Device Characterization and Functionality

To evaluate the performance and reliability of the OSmini platform, this study conducted a series of characterization experiments in both technical and biological contexts. The initial tests verified flow uniformity and assessed lateral diffusion across the porous membrane—two parameters critical for maintaining isolated drug delivery lanes and reproducible channel operation. Follow-up studies demonstrated the platform's ability to deliver fluorescent dyes to fixed and fresh PY8119 mouse tumor slices, revealing spatially resolved and time-dependent molecular diffusion. These experiments included single dye perfusion, co-delivery strategies, and localized delivery of a Doxorubicin gradient to model dose-dependent tissue responses. Together, these results validate the platform's capacity for multiplexed drug delivery, precise spatial control, and compatibility with live-tissue experimentation.

4.1 Flow Uniformity Characterization

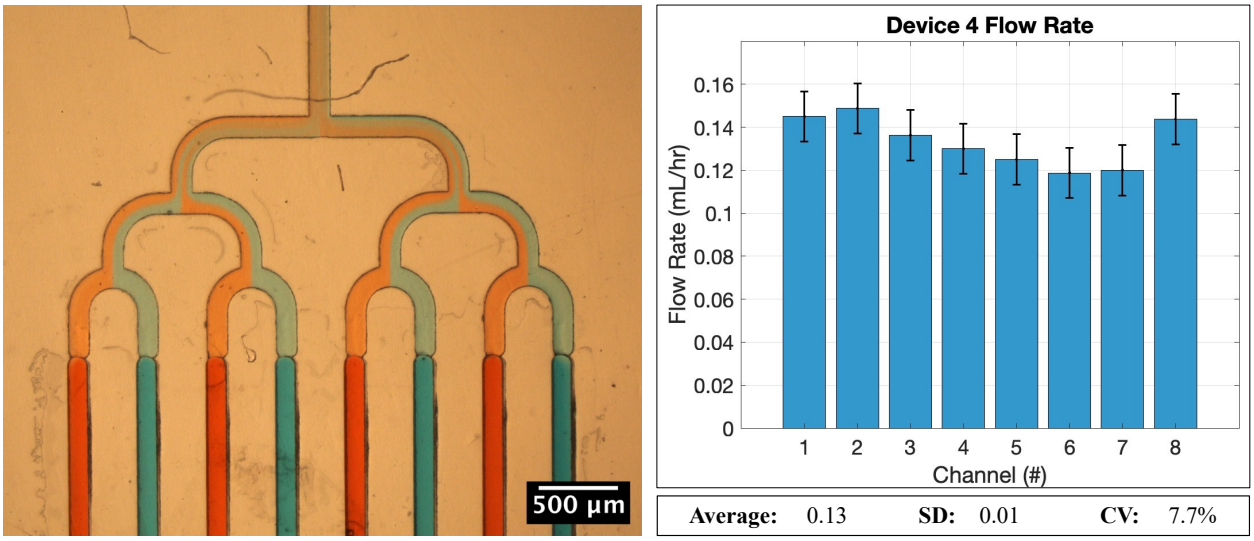

Figure 5. Flow uniformity characterization across channels. This image shows the OSmini device filled with alternating red and blue food dyes to visually assess uniform channel perfusion and isolation. The bar graph shows flow rates across all eight channels in a representative device, with error bars indicating standard deviation, demonstrating consistent and reproducible fluid delivery across the device.

To evaluate the consistency of channel fabrication and ensure reliable, reproducible fluid delivery across the OSmini platform, the experiment systematically assessed flow uniformity across multiple fabricated devices. The evaluation began with a qualitative assessment, which involved introducing alternating red and blue food dyes into adjacent inlet channels and visualizing the resulting flow patterns in the central culture region (**Fig. 5**). The separated colored lanes across the entire culture area confirmed successful channel isolation, with no observable leakage or cross-talk between adjacent flow streams, indicating a high degree of precision in the channel network fabrication.

After completing the qualitative evaluation, the experiment performed quantitative flow rate measurements to characterize the uniformity of fluid delivery across all channels. For each device, all inlet wells were filled with 2 mL of aqueous solution, and a syringe pump withdrew fluid at a rate of 1 mL/hr. Each device operated for 4 hrs to reach steady-state conditions and allow accurate volumetric measurements. The experiment collected and measured flow from individual channels by recording the displaced volume over the test period. As shown in **Fig. 5**, the eight delivery channels of Device 1 exhibited minimal variability, with an average flow rate of 0.13 mL/hr, a standard deviation of 0.01 mL/hr, and a coefficient of variation (CV) of 7.7%. This low CV reflects the successful balancing of hydraulic resistances within the microfluidic network and confirms that the current fabrication protocol consistently produces devices with reproducible fluidic performance.

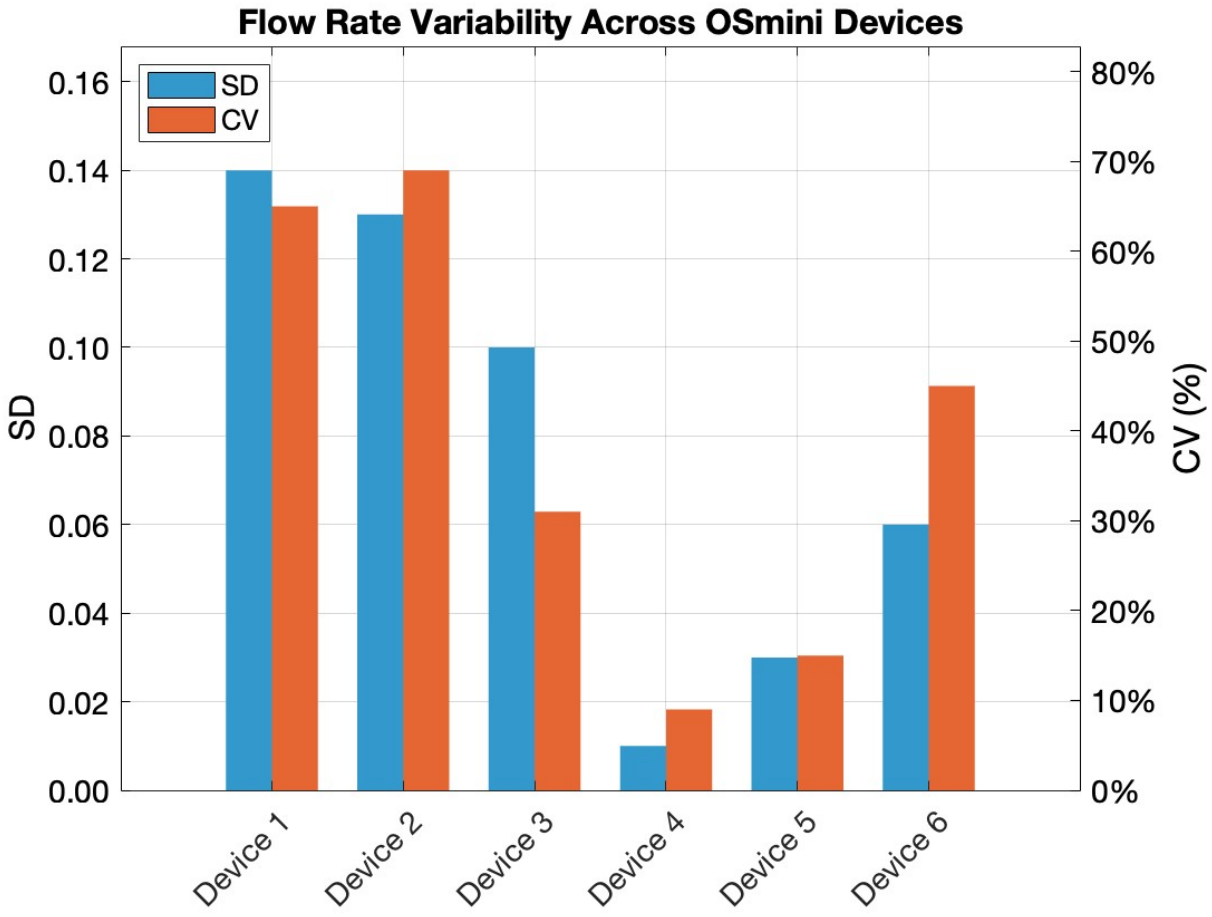

Figure 6. Flow rate variability across different OSmini devices.

Flow rate measurements were conducted on six independently fabricated OSmini devices under identical operating conditions to assess reproducibility across devices. The standard deviation (SD) and coefficient of variation (CV) were computed across all eight channels within each device and are summarized in **Fig. 6**. Devices 1 and 2 exhibited the highest variability, with SD values of ~0.14 mL/hr and CVs near 65–70%. These early devices were fabricated during initial protocol development, and the higher variability likely reflects imprecise alignment during bonding or channel deformation due to suboptimal sealing pressure. Device 3 showed moderate variability (SD = 0.10 mL/hr, CV ~30%), while Devices 4 and 5 demonstrated markedly improved uniformity, with SD values under 0.03 mL/hr and CVs below 10%, indicating successful refinement of the fabrication workflow. Device 6

presented moderate variability (SD = 0.06 mL/hr, CV ~45%), suggesting potential inconsistencies in bonding uniformity or debris obstruction in select channels.

Collectively, these results demonstrate that the OSmini platform achieves consistent and reproducible fluid delivery across its eight microfluidic channels. The dye-based qualitative assessment confirmed precise channel isolation without cross-contamination, indicating effective sealing and spatial control of flow. Quantitative flow rate measurements further validated this uniformity, with most devices exhibiting low standard deviations and coefficients of variation. While early-generation devices (e.g., Devices 1 and 2) showed higher variability likely due to fabrication imperfections, subsequent iterations (Devices 4 and 5) demonstrated substantial improvements in flow uniformity following protocol refinements. These findings underscore the robustness of the current fabrication process and highlight the importance of quality control during bonding and assembly to minimize flow variation. Ensuring tight flow rate tolerances across channels is critical for synchronizing treatment delivery, preserving experimental timing, and achieving reliable and interpretable results in downstream drug testing applications.

4.2 Lateral Diffusion Assessment using Fluorescein

Lateral diffusion through the porous membrane can lead to drug cross-talk between adjacent channels; assessing this effect is critical for preserving discrete spatial delivery—particularly at lower flow rates, which prolong run time but increase the risk of diffusion-induced mixing. To quantify the extent of lateral diffusion, the OSmini device was operated under controlled conditions using fluorescein as a model small molecule. Fluorescein was chosen because its molecular weight (MW, 332 g/mol) is similar to that of many small-molecule cancer drugs, making it relevant for studying diffusion behavior across the porous membrane. Channels 2 and 7 were loaded with 100 μM FITC solution, while all remaining channels were loaded with phosphate-buffered saline (PBS) as blank controls. This sparse loading configuration enabled isolated evaluation of diffusion away from individual delivery lanes into adjacent regions.

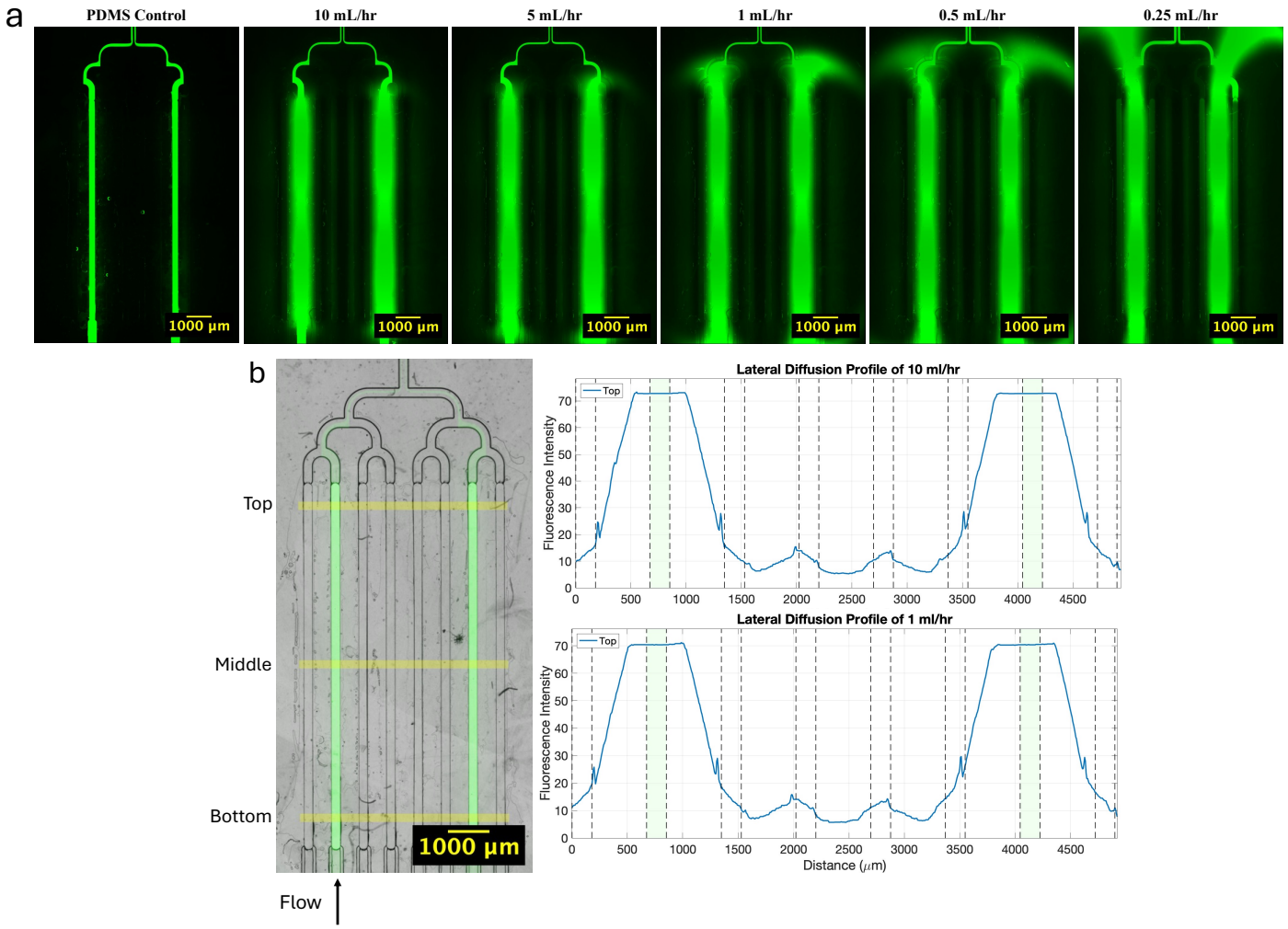

Figure 7. Lateral diffusion of fluorescein across the porous membrane at varying flow rates. (a) Fluorescence images show FITC-containing channels with increasing lateral diffusion into adjacent blank lanes as the flow rate decreases. A PDMS control blocks vertical diffusion, confirming that the signal in adjacent lanes results from membrane-based diffusion. (b) Brightfield image overlaid with fluorescence signal highlighting the three regions (top, middle, and bottom) selected for quantitative analysis. Representative lateral fluorescence intensity profiles across the porous membrane at 10 mL/hr (top graph) and 1 mL/hr (bottom graph), taken from the top region.

Devices were connected to a syringe pump and operated under seven different flow rates: 10 mL/hr, 5 mL/hr, 2 mL/hr, 1 mL/hr, 0.75 mL/hr, 0.50 mL/hr, and 0.25 mL/hr. After 10 min of steady-state flow at each flow rate, fluorescence imaging was performed to visualize fluorescein distribution. Fluorescence intensity profiles were acquired across the porous

membrane surface, spanning from the loaded FITC lanes into adjacent blank lanes, to quantify the degree of lateral spread.

Fluorescence analysis was performed by systematically extracting intensity profiles from three distinct vertical regions of each device: the top, middle, and bottom sections of the membrane relative to the channel network, **Fig. 7**b. This spatial separation was critical to assess whether lateral diffusion varied along the length of the device, potentially due to small pressure gradients or flow instabilities across the culture chamber. For each region, a line scan perpendicular to the direction of flow was used to quantify the fluorescence intensity distribution across. To ensure accurate and comparable fluorescence quantification across different flow conditions, two exposure settings were utilized for image acquisition: a short exposure of 8.5ms to avoid saturation in the highly fluorescent delivery lanes and a longer exposure of 80 to enhance the detection sensitivity for small amounts of fluorescein diffusion into neighboring lanes. This dual-exposure strategy allowed high-intensity regions (delivery lanes) and low-intensity regions (adjacent blank lanes) to be measured reliably within the dynamic range of the imaging system.

In addition, a control experiment was performed by sealing the open channels with a flat slab of PDMS instead of a porous membrane. In this setup, the device was operated at 10 mL/hr, and fluorescence imaging was performed under identical conditions to visualize the baseline distribution of fluorescein in the absence of lateral diffusion through a porous membrane. The PDMS-sealed control provided a reference profile showing the confinement of fluorescein within the delivery lanes without membrane-mediated spreading.

As shown in **Fig. 7**a, fluorescence images of the OSmini device at different flow rates revealed a progressive increase in lateral diffusion as the flow rate decreased. Quantitative fluorescence intensity profiles further confirmed this trend. At 10 mL/hr, intensity peaks corresponding to the loaded channels were sharp and distinct, and adjacent regions maintained low baseline fluorescence after background subtraction. In contrast, at 1 mL/hr, the intensity peaks were broader, and elevated fluorescence was detected between the loaded channels, indicating significant diffusion-driven cross-talk. These findings

demonstrate that lower flow rates, which prolong residence time within the porous membrane, promote lateral diffusion, and reduce spatial delivery precision.

To accurately quantify fluorescein distribution and lateral diffusion across the porous membrane, background correction was applied to all fluorescence intensity profiles before analysis. For each image, background subtraction was performed by identifying the minimum fluorescence intensity range within the field of view. This minimum intensity typically corresponded to regions distant from the fluorescein-loaded delivery lanes, where no significant FITC diffusion was expected. The identified background intensity was subtracted uniformly from all measurements across the profile, effectively zeroing the baseline fluorescence signal and removing contributions from ambient fluorescence, camera noise, and any low-level membrane autofluorescence. This approach ensured consistent and comparable intensity measurements across different flow conditions, exposure times, and device regions, enabling accurate quantification of lateral diffusion behavior.

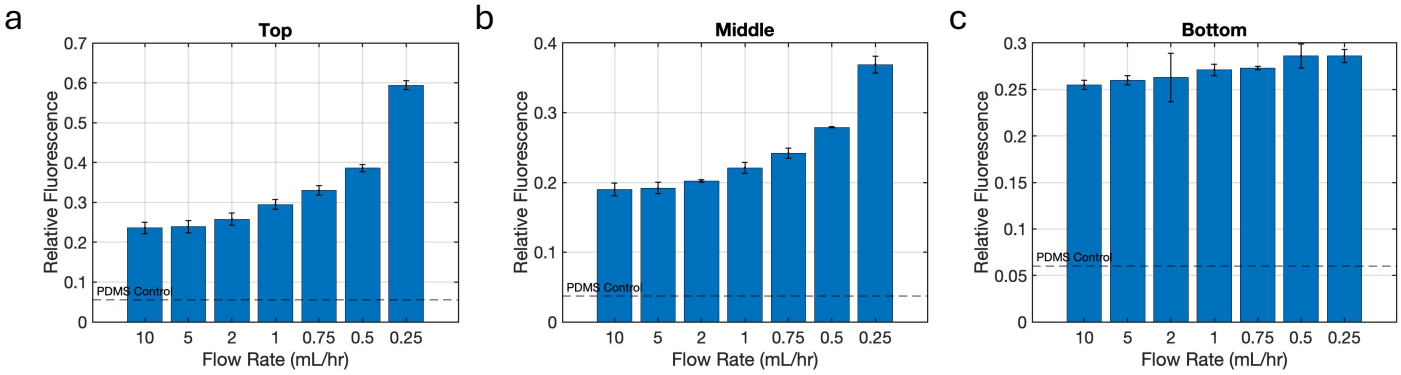

Figure 8. Quantification of lateral diffusion in top (a), middle (b), and bottom (c) regions, one channel away from the fluorescein delivery lane. Relative fluorescence intensity was measured at decreasing flow rates to assess spatial confinement. Dashed lines indicate PDMS control fluorescence levels, used to define background signal.

Following background correction, quantitative analysis of lateral diffusion was performed across the device's top, middle, and bottom regions as a function of decreasing flow rates. Quantitative comparison of background-corrected fluorescence profiles across the

device's top, middle, and bottom areas further confirmed the flow-dependent trends in lateral diffusion, **Fig. 8**. For all regions, the relative fluorescence intensity in adjacent blank channels increased progressively as the flow rate decreased from 10 mL/hr to 0.25 mL/hr, indicating enhanced diffusion-mediated cross-talk at lower flow rates.

At the top region, relative fluorescence levels remained low at higher flow rates (10 and 5 mL/hr). However, they showed a marked increase at flow rates below 2 mL/hr, reaching a maximum relative fluorescence of approximately 0.65 at 0.25 mL/hr. The middle region exhibited similar trends, although baseline relative fluorescence values were consistently lower than the top, particularly at flow rates above 1 mL/hr. Notably, both the top and middle regions displayed strong sensitivity to flow rate, with sharp increases in lateral diffusion as the flow rate decreased. This suggests that at lower flow rates, the extended residence time of fluorescein within the porous membrane significantly enhances lateral diffusion, disproportionately affecting these regions compared to the bottom of the device.

In contrast, the bottom region demonstrated relatively high lateral diffusion across all tested flow rates. Even at the highest flow rates of 10 and 5 mL/hr, the bottom region exhibited elevated relative fluorescence compared to the top and middle, suggesting persistent diffusion effects near the outlet zone of the device. At 0.25 mL/hr, relative fluorescence in the bottom region reached approximately 0.30, which, although lower than the top region at the same flow rate, remained significantly above the PDMS control baseline.

These findings indicate that while diffusion increases with decreasing flow rate, the degree of lateral spread is not uniform across the device. The top and middle regions are more susceptible to lateral diffusion than the bottom. To minimize cross-talk and maintain discrete spatial drug delivery, maintaining higher flow rates (>2 mL/hr) and optimizing flow uniformity across the entire culture area are critical design considerations.

Baseline fluorescence profiles obtained from the PDMS-sealed control were subtracted from each experimental condition to refine the analysis further and isolate flow-dependent diffusion effects. This subtraction removed the background signal from normal flow inside

the channels, allowing clear measurement of how much fluorescein spread through the membrane at different flow rates.

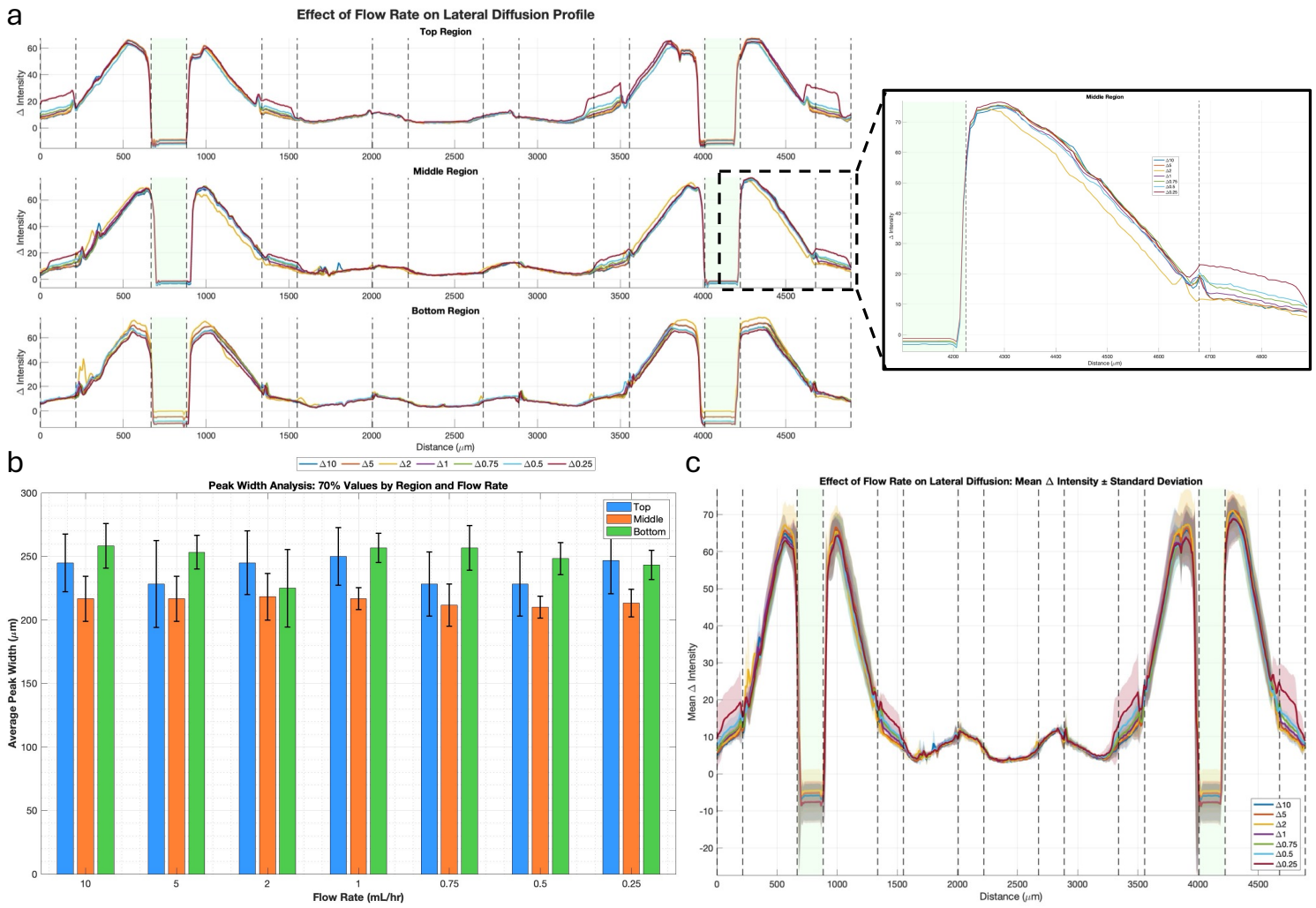

Figure 9. Comprehensive Analysis of Flow Rate Effects on Lateral Diffusion in Microfluidic Channels. (a) Δ intensity was calculated by subtracting the baseline signal from the PDMS control (no diffusion) from each experimental condition to isolate flow-dependent lateral diffusion. The inset shows a magnified view of peak 4 for the middle region, highlighting the detailed lateral diffusion profile and demonstrating how flow rate affects shape of compound distribution around this delivery channel. Vertical dashed lines indicate microfluidic channel boundaries, and colored traces represent different flow rate conditions as indicated in the legend. (b) Average peak widths at 70% maximum intensity across different flow rates for each spatial region. Error bars represent standard deviation across four peaks measured in each region. (c) Mean Δ intensity profiles (solid lines) averaged across

all three spatial regions with shaded bands representing ±1 standard deviation to quantify spatial variability.

The fluorescence intensity profile obtained from the PDMS-sealed control device was subtracted from the corresponding experimental profile acquired with the porous membrane in place for each experimental condition. This subtraction removed baseline channel fluorescence contributions associated with convective transport and allowed selective visualization of lateral diffusion caused specifically by molecular transport through the porous membrane. The resulting Δ intensity profiles represent the net lateral diffusion under different flow rates, corrected for non-diffusive signal contributions (**Fig. 9**).

Initial examination of individual regional profiles suggested potential flow rate dependencies, with apparent variations in peak sharpness and baseline intensities across different spatial regions of the device (**Fig. 9**a). In some regions, profiles corresponding to higher flow rates (10 and 5 mL/hr) appeared more sharply confined with steeper intensity gradients at channel edges, while lower flow rates seemed to exhibit broader diffusion patterns. The inset in **Fig. 9**a shows a magnified view of channel 7 for the middle region, illustrating the detailed lateral diffusion profile where subtle variations in peak shape across flow rates can be observed. However, these observations prompted a comprehensive statistical analysis to distinguish between genuine flow-dependent effects and spatial measurement variability inherent to the experimental system.

Peak width quantification provided the first indication of flow rate independence (**Fig. 9**b). Measurements at 70% maximum intensity across four distinct peaks in each region yielded average widths consistently ranging from 210-260 μm across all tested flow conditions (0.25-10 mL/hr), with standard deviations typically below 15-25 μm. The absence of systematic trends in peak width versus flow rate, combined with overlapping error bars across all conditions, demonstrates that lateral diffusion profiles are governed by the intrinsic transport properties of the porous membrane rather than convective flow parameters. Notably, the middle region (orange bars) showed the most consistent peak

widths across all flow rates, while top and bottom regions exhibited slightly more variation but still within overlapping confidence intervals.

Statistical analysis of averaged profiles across all three spatial regions confirmed this flow rate independence (**Fig. 9**c). Mean Δ intensity profiles, calculated by point-by-point averaging across the three regions, showed remarkably consistent peak shapes, amplitudes, and baseline behaviors across all flow conditions. The extremely tight standard deviation bands (shaded regions, typically <5% of peak intensity) indicate excellent spatial reproducibility within the device and demonstrate that regional variations are minimal compared to the signal magnitude. The overlapping confidence intervals of mean profiles across all flow rates provide strong evidence for flow rate independence in lateral diffusion behavior.

Contrary to initial observations suggesting flow rate dependence, the statistical analysis demonstrates that differences between individual regional measurements fall within the range of spatial measurement uncertainty. The shaded error bands in the averaged profiles show that flow rate effects are smaller than the natural spatial variation across the device, indicating that the system operates in a diffusion-dominated regime rather than a convection-influenced transport mode.

These findings establish that lateral diffusion performance remains robust across a wide operational flow rate range (0.25-10 mL/hr), providing flexibility for applications requiring different perfusion speeds without compromising spatial specificity. The flow rate independence observed through statistical analysis suggests that residence time variations within this range do not significantly impact molecular transport through the porous membrane, likely due to the dominance of diffusive over convective transport mechanisms. This operational flexibility is advantageous for applications requiring extended treatment durations, as flow rates can be adjusted for experimental convenience without affecting spatial drug delivery precision. More broadly, these results have important implications for the design and optimization of porous membrane-based microfluidic platforms for drug delivery and tissue engineering applications. The demonstrated robustness of diffusion-

mediated transport across a wide flow rate range suggests that such systems can be reliably scaled and adapted for diverse experimental protocols without requiring extensive re-optimization of flow parameters. This finding also validates the use of statistical averaging approaches for characterizing microfluidic device performance, providing a methodological framework that could be applied to other spatially heterogeneous systems where distinguishing genuine effects from measurement artifacts is critical for accurate performance assessment.

4.3 Fluorescent Dye delivery in Fixed PY8119 Mouse Tissue Slice

To assess the OSmini platform's ability to deliver multiple compounds spatially into the tissue, fixed PY8119 tumor slices were exposed to fluorescent dyes under controlled flow conditions. Fluorescein Isothiocyanate (FITC), Propidium Iodide (PI), and Hoechst 33342 were delivered through separate channels at a total device flow rate of 1 mL/hr for up to 4 hrs. Fluorescence imaging and quantitative intensity profiling were performed after 2 and 4 hrs of continuous delivery to characterize spatial distribution and stability over time.

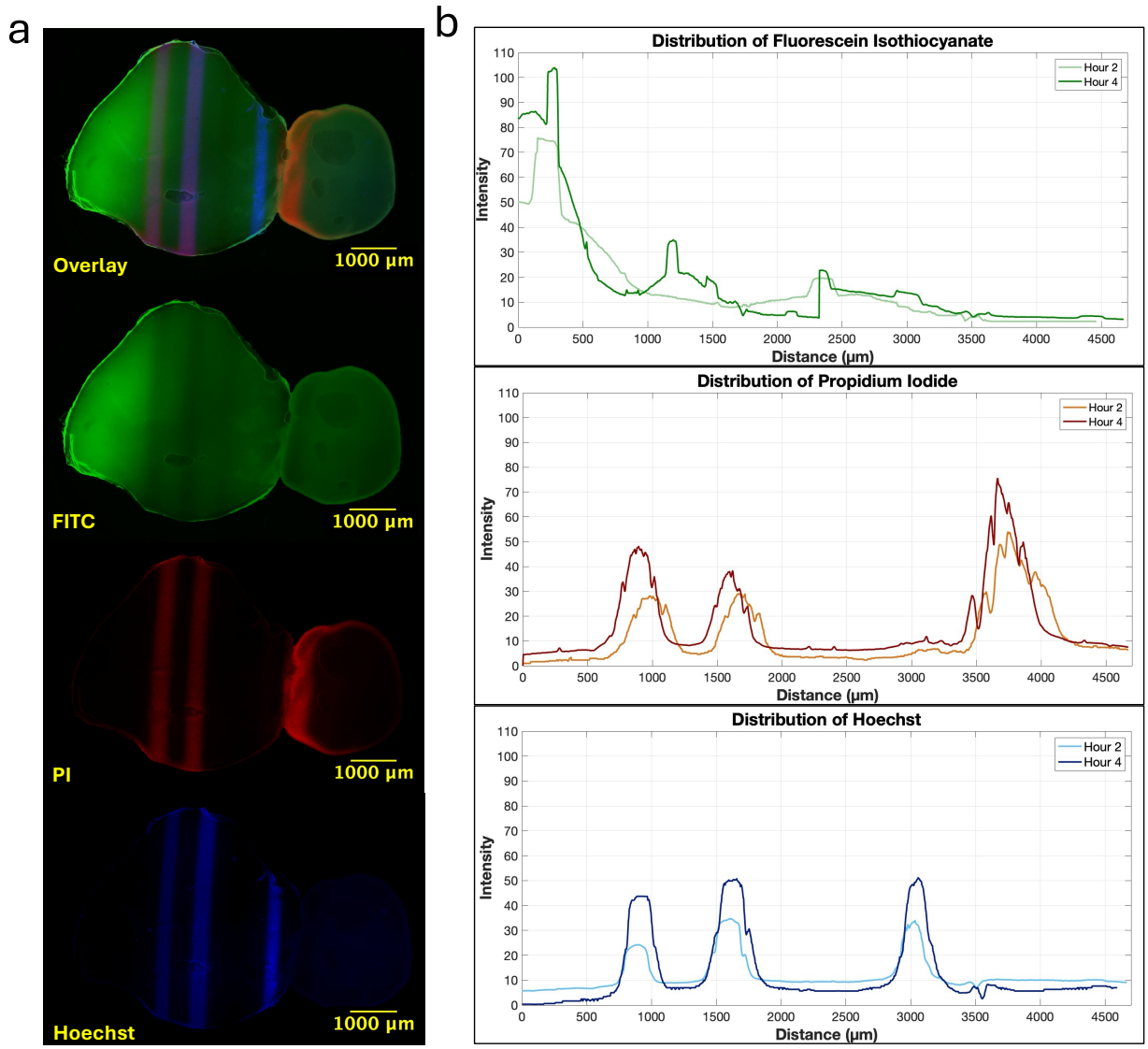

Figure 10. Distribution of fluorescent dyes in fixed PY8119 tumor tissue after 2 and 4 hrs of delivery. (a) Images show spatial delivery of Fluorescein Isothiocyanate, Propidium Iodide, and Hoechst in fixed PY8119 slices after exposure to fluorescent dyes at 4 hrs. (b) Intensity profiles for Fluorescein Isothiocyanate, Propidium Iodide, and Hoechst at 2-hr and 4-hr timepoints.

Tumor tissue from PY8119 was sliced into 250 µm-thick sections and immersed in 4% paraformaldehyde (PFA), which were then fixed to preserve cellular and structural integrity. Following fixation, slices were rinsed thoroughly with phosphate-buffered saline (PBS) to remove residual PFA and stored in PBS at 4°C until use. Before experiments, the fixed slices were gently blotted to remove excess buffer and carefully positioned onto the porous

membrane of the OSmini device, ensuring even contact across the channel interface for uniform dye delivery.

This experiment used three distinct fluorescent dyes to evaluate the OSmini platform's ability to deliver multiple compounds simultaneously and spatially across fixed tumor tissue. The dyes included FITC, PI, and Hoechst 33342. Stock solutions were diluted in sterile phosphate-buffered saline (PBS) to the following final concentrations: FITC at 100 µM, Hoechst at 16 µM, and PI at 10 µM. All dye solutions were prepared fresh before the experiment to avoid photobleaching or degradation. Each dye was loaded into specific inlet channels to ensure non-overlapping spatial distribution and enable comparison of repeated dye delivery patterns across non-adjacent lanes. The channel assignments for each dye are summarized in Table 7.

LANE	**1**	**2**	**3**	**4**	**5**	**6**	**7**	**8**
DYE	FITC	Hoechst	PI	FITC	Hoechst	PI	PBS	PBS

Table 6. Dye distribution across microfluidic lanes in the OSmini device for the multiplexed staining experiment.

After loading the fluorescent dye solutions into their respective inlet wells, the OSmini device was connected to a syringe pump, and the flow rate was set to 1 mL/hr. Delivery was maintained for up to 4 hrs at room temperature, with fluorescence imaging performed at 2-hr and 4-hr timepoints to compare dye intensity and spatial distribution over time.

Following dye delivery and imaging, fluorescence signals revealed distinct spatial patterns for each dye corresponding to the delivery channels. As shown in **Fig. 10**a, FITC, Propidium Iodide, and Hoechst exhibited strong fluorescence localized near the respective delivery lanes, confirming successful multiplexed dye delivery across the tissue surface. While the overlay image in **Fig. 10**a demonstrates generally discrete delivery regions, subsequent quantitative analysis revealed some cross-contamination between adjacent channels, particularly affecting PI and Hoechst distribution patterns.

To quantitatively evaluate the spatial resolution and temporal stability of fluorescent dye delivery across the tissue slice, intensity profiles were extracted from fluorescence images at both 2-hr and 4-hr time points for FITC, PI, and Hoechst. These line profile plots provide insight into how well the OSmini device maintains distinct delivery lanes over time and how each dye diffuses through the fixed tissue matrix under continuous flow.

For FITC, the fluorescence intensity profile revealed a strong initial peak near the delivery site, followed by a rapid decline in signal with increasing distance. Notably, while a second peak corresponding to the second FITC delivery lane was present at the 2-hr timepoint, it became nearly indistinguishable at 4 hrs. This loss of peak definition suggests substantial lateral diffusion, resulting in signal broadening and overlap with adjacent tissue regions. The disappearance of the second peak later indicates that the dye was no longer spatially confined to its original delivery lane and had spread into surrounding areas. This behavior can be attributed to FITC's relatively low molecular weight (389.4 g/mol) and high concentration (100 μM), which likely facilitated diffusion through the fixed tissue matrix during continuous exposure [18]. Although the tissue was fixed, the prolonged 4-hr flow allowed FITC to migrate laterally beyond its delivery zone, diminishing spatial resolution and compromising peak separability.

For Propidium Iodide (PI), the fluorescence intensity profiles at both 2-hr and 4-hr time points exhibited three prominent peaks rather than the expected two based on the lane assignments. This likely resulted from the unintended mixing between adjacent channels, specifically between lanes 2 (Hoechst) and 3 (PI), leading to partial overlap in their respective delivery zones. Despite this channel interference, the peaks remained well-resolved and increased in intensity and width at the 4-hr mark, suggesting that PI continued accumulating in the tissue with sustained exposure. The maintained spacing and consistent rise in signal intensity over time confirm successful dye penetration and confinement within defined regions, albeit with some loss of spatial fidelity likely due to inter-channel leakage. Since PI is membrane-impermeant and binds selectively to nucleic acids in fixed cells, its behavior aligns with controlled delivery and time-dependent diffusion in a static matrix.

For Hoechst, a similar three-peak pattern was observed, diverging from the expected two-peak distribution based on the dye's placement in lanes 2 and 5. This pattern, consistent with what was seen for PI, further supports the occurrence of cross-contamination between adjacent channels—likely at the interface between the porous membrane and tissue slice. Despite this inter-channel mixing, the Hoechst signal maintained its characteristic sharp and narrow peak morphology, particularly at the 2-hr timepoint, reflecting its high DNA-binding affinity and rapid nuclear localization. By the 4-hr timepoint, Hoechst intensity increased slightly, but the peak shape and position remained relatively stable, indicating minimal lateral diffusion compared to the other dyes. This result highlights the dye's strong binding properties and stable retention in fixed-cell nuclei.

Overall, these temporal intensity comparisons reveal that while all three dyes maintained discrete delivery channels throughout the experiment, their degree of lateral diffusion varied. FITC showed the most pronounced spread, likely due to its concentration and physicochemical properties; PI showed moderate diffusion and time-dependent accumulation; and Hoechst exhibited minimal lateral movement with strong confinement to delivery regions. These observations underscore the OSmini platform’s capacity to deliver multiple reagents in a spatially controlled manner, making it well-suited for multiplexed labeling or drug testing applications in both fixed and live tissue systems.

Additionally, tissue fixation significantly alters how fluorescent dyes interact with cellular components in ways that explain the diffusion patterns observed in your experiments. PFA fixation creates protein cross-links that affect each dye differently: FITC shows increased lateral diffusion in fixed tissue due to reduced binding specificity after fixation, allowing it to spread more freely through the fixed matrix [19]. Propidium iodide undergoes the most dramatic transformation, changing from a membrane-impermeant viability marker in live tissue to a general DNA stain in fixed samples. However, fixation can interfere with its DNA binding through histone cross-linking [20]. In contrast, Hoechst maintains consistent nuclear specificity in both fixed and live tissues due to its high DNA binding affinity, explaining its superior spatial confinement in these experiments [21]. These differential

effects on binding kinetics directly correspond to the varying degrees of lateral diffusion observed in these fixed tissue experiments.

4.4 Perfusion in Fresh PY8119 Mouse Tissue Slice

Following the evaluation of fluorescent dye delivery in fixed PY8119 tumor slices, subsequent experiments were conducted in fresh, viable tissue to assess the platform under physiologically relevant conditions. Unlike fixed samples, live tissue retains active transport mechanisms, cellular uptake, and intact permeability barriers, all of which influence dye diffusion and spatial confinement. Performing dye delivery on fresh slices allowed for the characterization of real-time perfusion dynamics and provided insight into how tissue viability affects spatial precision and compound retention. This transition was essential for validating the OSmini platform's utility in live tissue applications, such as functional drug testing.

Fresh tumor tissue was harvested from mice bearing PY8119 tumors once tumors reached the appropriate size for experimental use. Immediately after excision, tumors were handled under sterile conditions to minimize contamination. Necrotic regions and surrounding non-tumor tissues were carefully dissected away to enrich viable tumor areas. Viable tumor pieces were embedded in 2% low-melting agarose to provide mechanical stability during sectioning. Using a vibratome, the agarose-embedded tumors were sectioned into slices of 250 μm thickness, maintaining consistent thickness to preserve tissue structure and minimize mechanical damage. Following sectioning, four slices were transferred onto two 0.4 μm transwell membrane inserts, with two slices per membrane. The inserts were then placed into a 6-well plate containing DMEM/F12 medium supplemented with heat-inactivated fetal bovine serum (HI FBS) to support slice viability. The slices were cultured at 37°C in a humidified incubator, and fresh media was added every 2–3 days. These prepared slices provided viable, reproducible samples suitable for controlled perfusion and drug delivery studies using the OSmini microfluidic platform.

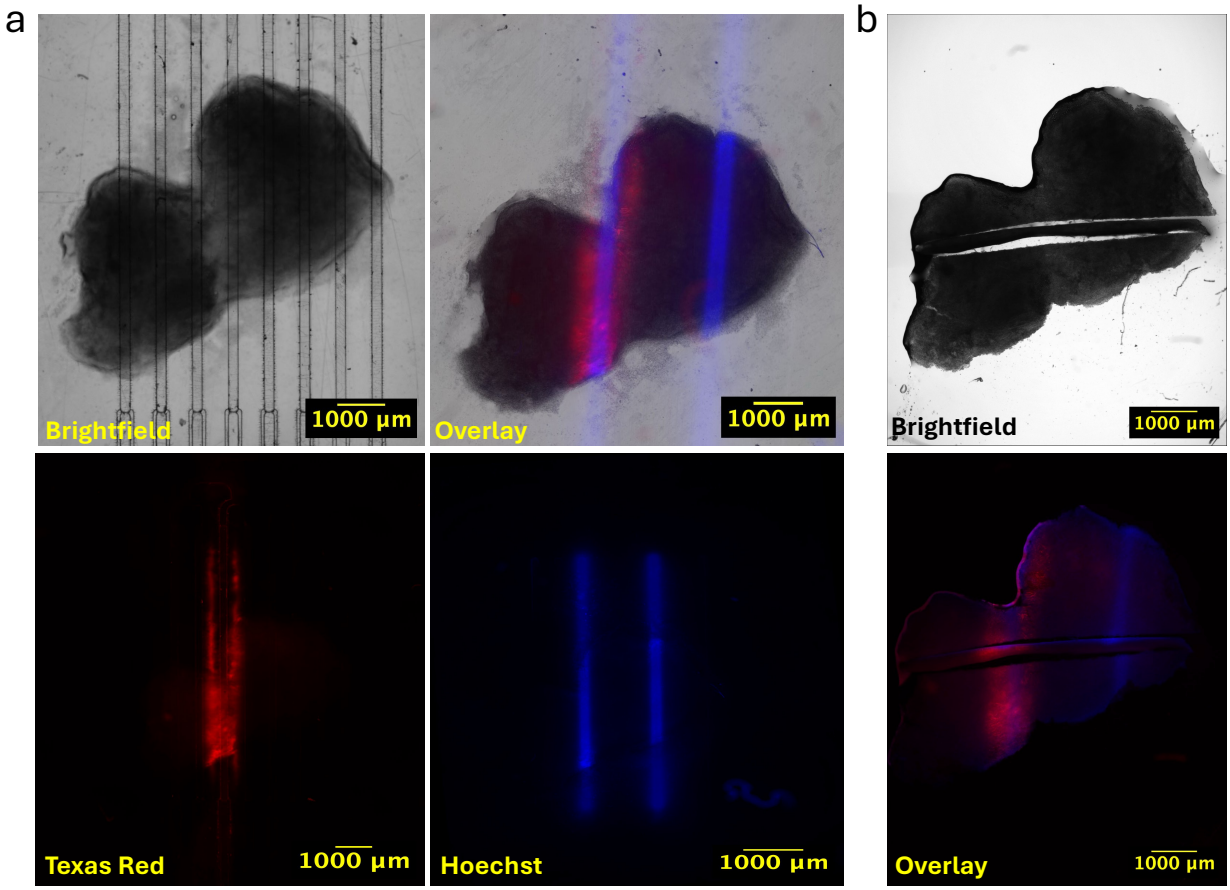

Figure 11. Spatial delivery of Texas Red and Hoechst dyes into live PY8119 tumor slices. (a) To assess spatial delivery and dye overlap, Hoechst (blue) was delivered alone in one lane and co-delivered with Texas Red (red) in another to evaluate multiplexed delivery and potential overlap. (b)The right panel shows an attempt at creating cross-sections of the tissue slice to demonstrate internal dye penetration and retention following delivery.

Texas Red and Hoechst 33342 were selected for this experiment to assess how small molecules of differing molecular weights distribute through live PY8119 tumor tissue. Hoechst, a low molecular weight (615.99 g/mol), membrane-permeable nuclear dye, was used to examine intracellular uptake and baseline tissue penetration [22]. In contrast, Texas Red (MW 625.2 g/mol), a larger, membrane-impermeant fluorophore, was chosen to evaluate extracellular spread and spatial confinement [23]. To compare transport behaviors in parallel, these dyes were delivered through separate microfluidic lanes on the OSmini3 device—Hoechst alone in one lane and a combination of Texas Red and Hoechst in another.

The primary objective was to determine how molecular size influences diffusion dynamics and penetration depth in viable tissue under continuous flow. Tumor slices cultured on transwell membranes were perfused for 4 hrs at room temperature at a total flow rate of 1 mL/hr, then imaged both before and after washing to assess fluorescence localization.

Following perfusion, residual media and dye solutions were removed, and each inlet well was flushed with PBS. Fluorescence images were acquired directly on the device using a Keyence BZ-x810 microscope to evaluate surface-level dye distribution. This motorized microscope automatically stitches images taken at high resolution, thus allowing for high-resolution imaging over large areas. The transwell insert was subsequently transferred to a 6-well dish and washed with PBS using a shaker for two 5-min intervals to remove unbound dye. Additional imaging was performed post-wash to evaluate signal retention. The tissue was then fixed in 4% paraformaldehyde by adding 1 mL beneath the transwell and 0.5 mL on top of the slices. Plates were sealed in parafilm and foil and incubated overnight at 4°C. After fixation, the slices were rinsed and equilibrated in 30% sucrose (in PBS) to prevent ice crystal formation during freezing. The tissue was then transferred to a petri dish, and a cross-section was cut and rotated onto its side to visualize the vertical dye penetration profile. The cross-section was imaged using the BZ-x810 to assess the internal diffusion depth and spatial confinement of the delivered dyes. This experiment directly compared small molecule transport through live tumor tissue and served as a functional benchmark for evaluating the OSmini platform's spatial delivery performance under biologically relevant conditions.

Fluorescence imaging after 4 hrs of perfusion revealed distinct differences in the spatial distribution of Hoechst and Texas Red in live PY8119 tumor slices. As shown in **Fig. 11**a, Hoechst fluorescence appeared as two well-defined bands corresponding to the delivery lanes, indicating strong nuclear uptake and limited lateral spread. In contrast, Texas Red fluorescence was markedly more diffuse, lacking the clear confinement observed with Hoechst. Due to its larger size and membrane-impermeant nature, this suggests that Texas Red may have experienced limited tissue retention or was more susceptible to washout

during the post-perfusion rinsing steps. The absence of a sharp, localized signal from Texas Red also implies that it may have diffused across the tissue surface. These results highlight the influence of molecular properties—such as membrane permeability and binding affinity—on spatial localization and signal persistence.

A cross-sectional imaging approach was attempted to evaluate the depth of dye penetration and spatial confinement within the tissue. The perfused tumor slice was carefully sectioned horizontally through its mid-plane and rotated onto its side to expose the vertical axis of dye transport. This orientation allowed for direct visualization of how far each dye penetrated from the surface into the tissue interior. While fluorescence from Hoechst and Texas Red was visible and appeared distributed throughout the tissue's thickness, the section's spatial orientation could not be definitively verified. As a result, no quantitative depth analysis was performed. Due to this uncertainty in tissue orientation and the absence of structural markers to confirm the flipped configuration, this cross-sectional view was used qualitatively to inspect signal presence rather than to extract precise diffusion profiles. Despite these limitations, the cross-section attempt provided preliminary insight into relative dye localization and highlighted the practical challenges of obtaining reliable vertical transport measurements in live tissue.

In summary, these experiments demonstrated that the OSmini platform can achieve spatially resolved delivery of small molecules in live tumor tissue, with molecular weight and membrane permeability playing key roles in diffusion and retention. While Hoechst exhibited localized uptake and consistent nuclear labeling, Texas Red showed more diffused distribution. The cross-sectional attempt offered qualitative insight into vertical penetration but underscored the technical challenges of obtaining precise depth-resolved data in soft, viable tissues. These findings establish a foundation for applying the platform to functional assays involving live tissue, including multiplexed drug delivery and pharmacodynamic studies.

4.5 Tissue Perfusion Assessment using Doxorubicin and Hoechst

The ability to deliver therapeutic agents with precise spatial control is a critical challenge in cancer treatment, where drug distribution heterogeneity can significantly impact treatment outcomes. Building upon the previously established capabilities of the OSmini platform for maintaining tissue viability and monitoring metabolic activity, this section explores the platform's potential for controlled spatial delivery of chemotherapeutic agents. By evaluating Doxorubicin perfusion through fresh PY8119 tumor tissue slices, this experiment addresses a key translational application of the microfluidic system: creating defined drug concentration gradients that mimic the heterogeneous exposure observed in tumors *in vivo*. To assess the OSmini platform's ability to deliver chemotherapeutic agents, a Doxorubicin gradient spatially was applied to fresh PY8119 tumor slices. The primary goal of this experiment was to evaluate how Doxorubicin diffuses through live tissue under continuous flow and whether distinct concentration-dependent effects could be observed across the delivery lanes. A gradient configuration was selected to mimic heterogeneous drug exposure, enabling the analysis of localized tissue penetration at varying Doxorubicin concentrations. Hoechst 33342 was delivered in a separate channel as a nuclear counterstain to mark cellular regions and assist with spatial tissue registration relative to the microfluidic architecture. Together, this experiment aimed to characterize how drug diffusion is influenced by concentration gradients and tissue viability, providing a proof-of-concept for OSmini's application in spatially controlled drug screening and perfusion-based pharmacodynamic studies.

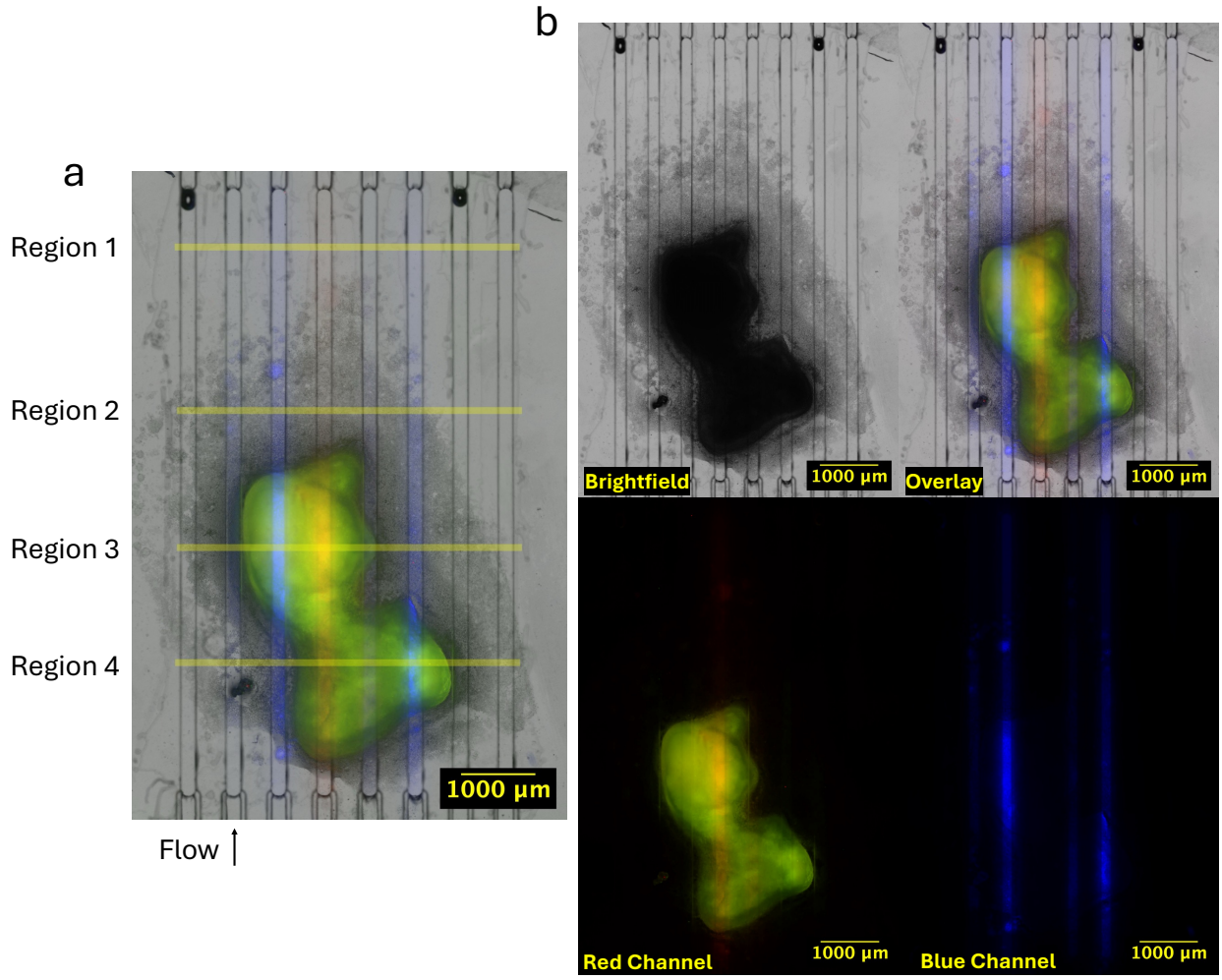

Figure 12. Spatial drug delivery assessment in PY8119 mouse breast tumor tissue using the OSmini platform. (a) Tumor slice with defined measurement regions showing Hoechst (blue) and Doxorubicin (red) distribution. Regions 1-4 indicate locations of intensity profile measurements across the tissue. Flow direction is indicated by the arrow. (b) Channel-specific visualization of drug penetration: brightfield image (top left), overlay of all channels (top right), combined green/red fluorescence showing tissue autofluorescence and Doxorubicin signal (bottom left), and Hoechst signal in blue channel (bottom right).

Fresh PY8119 tumor tissue was sectioned into 250 µm slices using a vibratome. Two slices were selected for the experiment and placed on 0.4 µm pore size transwell inserts positioned in 6-well culture plates. The tissue slices were initially maintained in an incubator at 37°C with 5% CO_2 to ensure tissue viability before the perfusion experiment.

The OSmini device was cleaned by spraying 70% ethanol to ensure sterility for the experiment. Following sterilization, the microfluidic channels were sequentially primed to remove air bubbles and establish proper flow conditions. First, deionized (DI) water was flushed through all channels, and the lines were temporarily clipped to prevent backflow. Subsequently, the channels were primed with autoclave-sterilized water, followed by Dulbecco's Phosphate-Buffered Saline (DPBS), and finally, with culture media. Visual inspection was performed at each step to confirm the complete removal of air bubbles from the microfluidic network, as bubbles could disrupt flow patterns and compromise experimental results.

A multi-channel syringe pump was calibrated to deliver a constant flow rate of 1 mL/hr throughout the experiment. This flow rate was selected to maintain physiological fluid dynamics while ensuring sufficient delivery of the compounds to the tissue. The fluidic lines were filled with DI water and secured with clips to prevent unwanted fluid movement before experimental initiation. Three solutions were prepared for the spatial drug delivery experiment to assess differential tissue penetration. The 1× Doxorubicin solution was prepared by diluting the stock concentration with HFH (HEPES-buffered F12/Ham) media to achieve the desired concentration and a final volume of 12 mL for consistent delivery throughout the experiment. For creating a concentration gradient, a 0.5× Doxorubicin solution was similarly prepared by diluting with HFH media to a final volume of 6 mL, enabling direct comparison of concentration-dependent tissue penetration across adjacent microfluidic lanes. Hoechst 33342 nuclear stain was diluted in HFH media to a final volume of 12 mL, providing sufficient volume for consistent nuclear counterstaining in lanes 3 and 6, which served as spatial reference points for tissue alignment and cellular distribution assessment.

The tumor tissue slice was carefully positioned on the OSmini device. To accommodate the tissue, slice adequately, the feet of the transwell insert were clipped off, allowing direct contact between the membrane-supported tissue and the microfluidic architecture. A spatial gradient configuration was established by introducing the Hoechst solution in lanes

3 and 6, the 1× Doxorubicin solution in lane 4, and the 0.5× Doxorubicin solution in lane 5, as shown in **Fig. 12**. This arrangement enabled simultaneous evaluation of different drug concentrations and provided spatial registration through nuclear staining. The system was placed in an incubator at 37°C with 5% CO_2 to maintain physiological conditions throughout the experiment. The tissue was perfused continuously for 6 hrs at a 1 mL/hr flow rate, providing sufficient time for drug penetration while preserving tissue viability. Following perfusion, fluorescence imaging was performed to capture the spatial distribution of Hoechst and Doxorubicin.

Fluorescence imaging after the 6-hr perfusion period revealed distinct patterns of compound distribution across the tissue. Notably, morphological changes were observed in the tissue following perfusion. Cells were observed to have migrated outward from the original tissue boundaries, as seen in **Fig. 12**b, likely due to the tumor cells' inherent migratory behavior when maintained under continuous flow conditions and in response to the concentration gradients of the delivered compounds. The Hoechst nuclear stain (blue) demonstrated effective penetration in lanes 3 and 6, where it was directly applied, providing a clear visualization of cellular distribution and tissue architecture. However, the lateral diffusion of Hoechst was detected in the adjacent left channel, with unintended traces visible beyond its primary delivery lane. This unwanted lateral migration indicates potential channel isolation limitations that could compromise compound delivery's spatial control. Such cross-channel contamination highlights the need for further optimization of the microfluidic architecture to ensure more precise spatial confinement of compounds. Despite this limitation, the Doxorubicin signal (red) showed the expected concentration-dependent penetration pattern, with stronger fluorescence visible in lane 4 (1× concentration) compared to lane 5 (0.5× concentration), consistent with the experimental gradient design.

To quantitatively assess spatial compound distribution across the tissue, fluorescence intensity profiles were extracted from the defined regions of interest (ROIs) using ImageJ. Separate profiles were generated for Hoechst and Doxorubicin. For Hoechst, raw intensity

values were directly measured from the blue fluorescence channel within each ROI, providing a readout of nuclear labeling efficiency and enabling evaluation of dye penetration across the tissue. A normalization approach was applied for Doxorubicin to correct for variability in tissue thickness and autofluorescence. Specifically, pixel-wise intensity values from the red channel (Doxorubicin signal) were divided by the corresponding values from the green channel, which captured tissue autofluorescence and served as a proxy for local tissue content. This red-to-green ratio produced a normalized intensity profile representing Doxorubicin uptake per unit of tissue signal. Using this normalization method, the analysis accounted for spatial heterogeneity in tissue properties. It ensured that observed differences in Doxorubicin fluorescence reflected true variations in drug penetration and retention rather than imaging artifacts or differences in tissue morphology.

For quantitative drug penetration and distribution analysis, four distinct regions of interest (ROIs 1-4) were strategically selected across the sample, as shown in **Fig. 12**a. ROI 1 was positioned at the very top to capture baseline fluorescence levels from the membrane. This region was crucial for establishing the background signal, which was subsequently subtracted from measurements in all other ROIs to obtain accurate fluorescence values attributable solely to tissue uptake of the compounds. This background subtraction methodology eliminated confounding factors such as autofluorescence from the membrane or non-specific binding of dyes to the transwell material. ROI 2 was designated to measure cellular labeling efficiency by focusing on areas where individual cells were distinguishable. This region served as a representative zone of active dye penetration into viable cells and was used to assess how robustly each compound labeled the tissue in the context of flow-based delivery. ROI 2 provided direct insight into both Hoechst and Doxorubicin's cellular localization and binding, especially in channels where compound delivery was intentional.

ROIs 3 and 4 were defined over the two distinct tumor slices positioned side-by-side on the OSmini platform. ROI 3 was located over the top slice, while ROI 4 was positioned over the bottom slice. These ROIs were selected to evaluate potential variability in compound

delivery and tissue labeling across different tissue replicates under identical flow conditions. By incorporating ROIs on both tissue sections, the analysis captured any heterogeneity in signal intensity due to slice positioning, tissue integrity, or localized flow differences within the microfluidic architecture. Additionally, comparison between ROIs 3 and 4 enabled the assessment of consistency in perfusion-based delivery between two spatially separated yet simultaneously treated tissue sections.

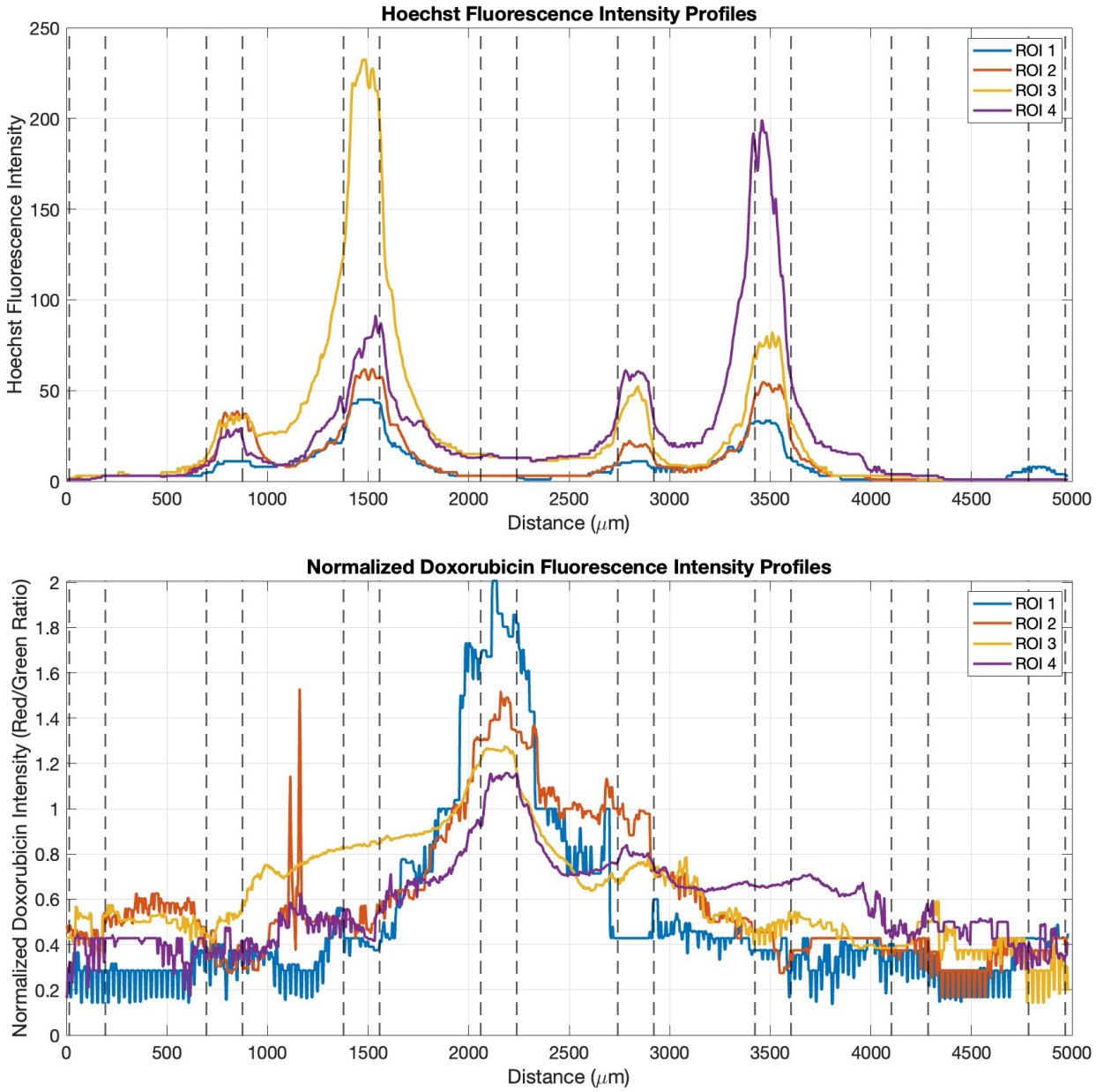

*Figure 13. Fluorescence intensity profiles across the tissue region extracted from the four defined regions of interest (ROIs) in **Fig. 12**a. (Top) Hoechst fluorescence intensity (blue channel). (Bottom) Normalized Doxorubicin intensity (red/green ratio). Dashed vertical lines represent the edges of the eight microfluidic delivery lanes. Distinct peaks in both Hoechst and Doxorubicin signals correspond to delivery lanes and cellular uptake zones, with stronger signals near central delivery positions.*

As shown in **Fig. 13**, fluorescence intensity profiles were extracted across the four regions of interest (ROIs) defined in **Fig. 12**a to evaluate the spatial delivery of Doxorubicin and

Hoechst 33342. The top panel displays Hoechst fluorescence intensity (blue channel), revealing strong, well-defined peaks at approximately ~1500 µm and ~3900 µm, corresponding to direct delivery lanes (lanes 3 and 6). These peaks confirm effective nuclear staining where Hoechst was actively perfused. However, in all ROIs, smaller secondary peaks appear just to the left of the primary delivery positions. These minor signals suggest lateral diffusion of Hoechst into adjacent channels, particularly toward the left side of each perfused lane. This asymmetric spread indicates imperfect channel isolation and reflects a slight degree of cross-lane contamination, which was also observed qualitatively in the raw fluorescence images. Despite this asymmetry, the spatial localization remains largely intact, with Hoechst staining predominantly confined to the intended lanes.

In the bottom panel, normalized Doxorubicin intensity—calculated as the ratio of red-to-green fluorescence to account for tissue autofluorescence—reveals a broad, centralized peak across all ROIs, with the highest intensity centered at approximately ~2100 µm. This peak aligns with lane 4, where 1× Doxorubicin was delivered, and represents the region of greatest drug penetration and accumulation. Adjacent to this central peak, a more modest rise in fluorescence is observed around ~3000 µm, corresponding to lane 5, where 0.5× Doxorubicin was applied. The clear distinction in peak heights between lanes 4 and 5 confirms successful gradient formation and illustrates a concentration-dependent uptake pattern. The gradual decline in intensity on either side of the main peak reflects diffusion-driven spread from the delivery lanes, with signal diminishing as distance from the source increases. Together, the Hoechst and Doxorubicin profiles in **Fig. 13** validate the OSmini platform's capability for spatially controlled compound delivery while also highlighting the need for fine-tuning lateral confinement.

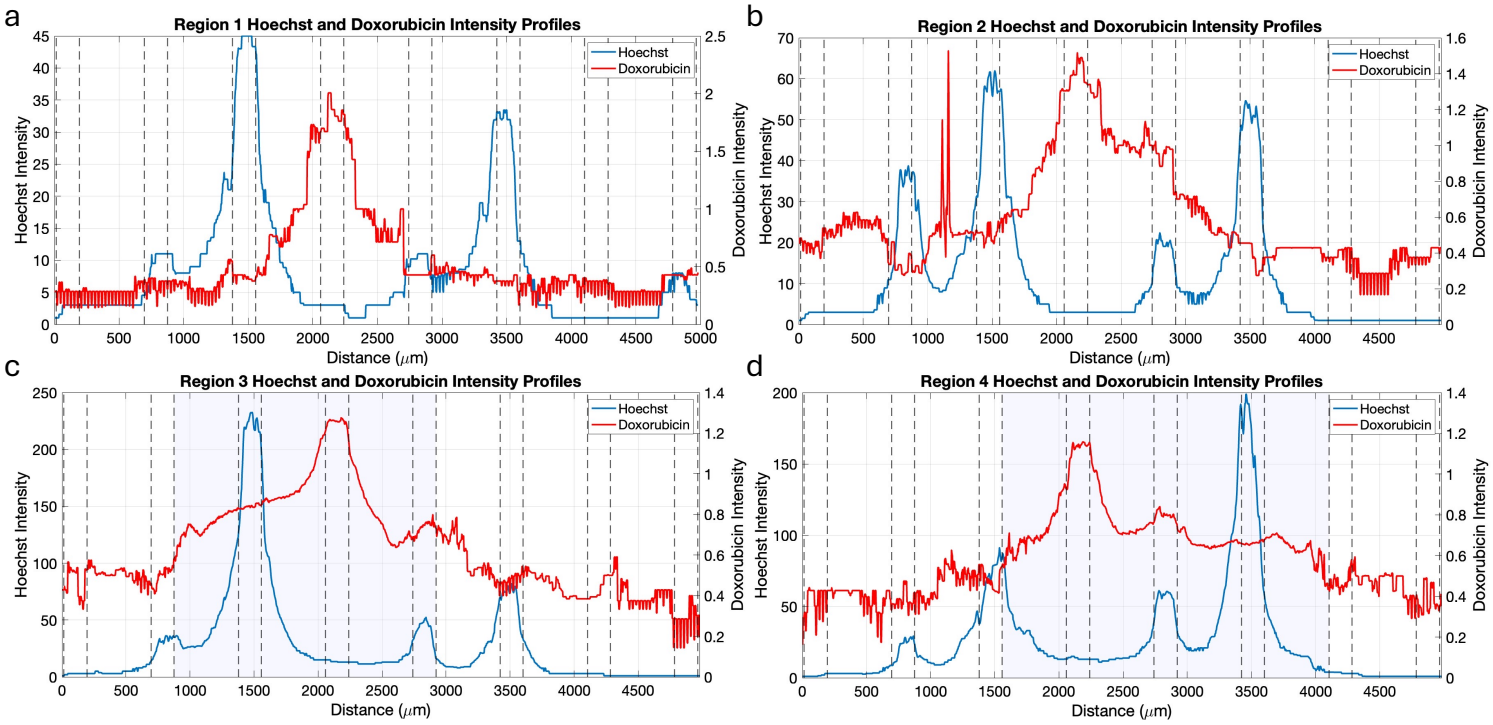

Figure 14. Region-specific fluorescence intensity profiles for Hoechst and Doxorubicin across different regions of the open microfluidic channels within the OSmini device. Four panels (a-d) show fluorescence intensity measurements from distinct regions of interest: (a) ROI 1, (b) ROI 2, (c) ROI 3, and (d) ROI 4. Each graph displays intensity plotted against Distance (μm), with blue lines representing Hoechst nuclear stain and red lines showing normalized Doxorubicin signal. Dashed vertical lines indicate the boundaries of the eight microfluidic delivery lanes. The blue highlighted background indicates tissue placement within the device.

To further characterize the spatial delivery performance of the OSmini platform, region-specific fluorescence intensity profiles of Hoechst and Doxorubicin were extracted from four distinct cross-sections along the open microfluidic channel array (**Fig. 14**a–d). Each plot captures a different region of the device over the eight delivery lanes, with dashed vertical lines indicating the microfluidic channel boundaries. The blue-shaded background in **Fig. 14**c and **Fig. 14**d indicates the region where tissue was placed on the device. ROI 1 (**Fig. 14**a) served as a baseline control, as it exhibited fluorescence primarily from the underlying Transwell membrane. As no tissue was present in this region, the fluorescence signal from both Hoechst and Doxorubicin represents background accumulation or membrane-associated signal. The fluorescence signals from all ROIs (1-4) represent the

combined contribution of compound accumulation on the membrane surface and any cellular/tissue uptake, providing a comprehensive view of drug distribution across different regions of the device.

In ROI 1 (**Fig. 14**a), the Hoechst signal exhibited two sharp peaks centered around 1500 µm and 3400 µm, aligning with microfluidic lanes 3 and 6, which were designated for Hoechst delivery. These peaks result from the accumulation of nuclear stain on the membrane surface in the absence of cells or tissue. Smaller Hoechst elevations around 800 µm and 2800 µm suggest minor lateral diffusion from the primary delivery lanes into adjacent channels. The Doxorubicin signal showed a distinct peak at around 2100–2500 µm, corresponding to lane 4, which received 1× Doxorubicin delivery. A slight elevation was also observed near lane 5, which was assigned the 0.5× Doxorubicin dose. These profiles demonstrate that fluorescent compounds accumulate on the porous membrane surface even in the absence of tissue, with signal magnitude reflecting both the membrane-binding properties of each compound and the efficiency of fluorescence detection on the flat membrane surface.

ROI 2 (**Fig. 14**b) captured fluorescence signals from a region peripheral to the main tumor tissue, where cells had migrated outward into adjacent microfluidic lanes during perfusion. This cellular migration is evidenced by the presence of Hoechst-positive nuclei and enhanced Doxorubicin signal in the fluorescence profiles. The Hoechst signal displayed distinct peaks around 1500 µm and 3400 µm, aligning with delivery lanes 3 and 6, consistent with nuclear labeling of scattered, outward-migrated cells. Additional Hoechst peaks in neighboring channels further support the presence of dispersed cells or lateral dye diffusion. The Doxorubicin signal profile showed markedly different characteristics compared to the membrane-only control. A clear peak emerged around 2100-2400 µm corresponding to lane 4 (1× Doxorubicin dose). This represents a substantial enhancement over the baseline membrane accumulation observed in ROI 1, indicating active cellular uptake by the migrated cell population. A secondary, smaller peak was detected around lane 5 (0.5× Doxorubicin), demonstrating dose-dependent uptake even in this sparse

cellular environment. The Doxorubicin signal also exhibited a broader baseline elevation across the 1500-3000 μm range, suggesting that the migrated cells retained and concentrated the drug beyond the immediate delivery channels. This pattern indicates that even relatively sparse, outward-migrated cells possess sufficient metabolic activity and membrane transport capacity to accumulate measurable quantities of Doxorubicin, distinguishing cellular uptake from simple membrane surface binding.

ROI 3 (**Fig. 14**c) was positioned over the central region of the top tissue slice and exhibited the strongest and most well-defined fluorescence signals across all measured parameters, indicative of optimal perfusion conditions and robust tissue-device interface. This region represents the core tumor tissue with high cellular density and maintained tissue architecture. The Hoechst fluorescence profile in ROI 3 demonstrated exceptionally strong nuclear labeling with sharp, well-defined peaks, corresponding to delivery lanes 3 and 6 respectively. The peaks exhibited steep rise and fall profiles with minimal baseline spreading, indicating precise spatial localization of the nuclear stain within the targeted delivery channels. Notably, the Hoechst signal showed minimal lateral diffusion between channels, suggesting that the dense tissue matrix effectively confined the dye to its intended delivery zones while maintaining efficient cellular uptake. The Doxorubicin distribution pattern in ROI 3 revealed complex penetration dynamics within the tissue environment. Primary peaks were observed at lane 4 (1× Doxorubicin) and lane 5 (0.5× Doxorubicin), demonstrating clear dose-dependent accumulation. Unlike the sharp, confined peaks observed with Hoechst, the Doxorubicin signal exhibited a characteristic broad elevation, creating an elevated baseline across multiple microfluidic channels. This extensive lateral distribution suggests active intratissue diffusion, where Doxorubicin molecules penetrate beyond the immediate delivery channels and distribute throughout the tissue matrix via intercellular transport mechanisms. The sustained elevation between delivery lanes indicates that the dense cellular environment promotes drug retention and redistribution, consistent with Doxorubicin's known affinity for binding to cellular components including DNA and various intracellular structures. Additionally, a notable secondary elevation was observed in the 900-1800 μm region, despite this area not being directly above a Doxorubicin

delivery lane, further supporting the concept of significant lateral drug migration within the tissue architecture.

Similar results were observed for ROI 4 (**Fig. 14**d) which was positioned over the central region of the bottom tissue slice. Hoechst fluorescence showed clearly defined peaks at delivery lanes 3 and 6, confirming that nuclear labeling occurred effectively in this region. The Doxorubicin signal profile, in contrast, showed broad and elevated fluorescence across multiple regions. Again, dose-dependent peaks at lane 4 (~2100 µm, 1× Doxorubicin) and lane 6 (~3500 µm, 0.5× Doxorubicin) were seen. A broad elevation across the 1500-4000 µm range indicated extensive lateral drug diffusion within the tissue matrix. ROI 4 exhibited more pronounced asymmetric distribution compared to ROI 3, with signal extending beyond 3500 µm toward the device periphery, likely reflecting edge effects or variations in tissue architecture. Overall signal intensities were modestly lower than ROI 3 (10-15% reduction), possibly due to reduced perfusion efficiency at greater tissue depth. The sustained elevation in non-delivery regions demonstrates the tissue's capacity for drug redistribution through intercellular transport mechanisms.

The experimental results demonstrate clear differences in fluorescence patterns between membrane-only regions (ROI 1), cell-sparse peripheral areas (ROI 2), and dense tissue regions (ROIs 3-4). The consistently lower fluorescence intensity of Doxorubicin compared to Hoechst across all regions arises from fundamental differences in their intrinsic fluorescence properties and cellular uptake characteristics. Doxorubicin has a substantially lower fluorescence efficiency, exhibiting a quantum yield of only 5–10% in aqueous environments, whereas Hoechst dyes are specifically engineered for bright nuclear staining and achieve significantly higher quantum yields upon binding to DNA [24]. The disparity is further amplified by differences in cellular uptake kinetics. Hoechst dyes are optimized for rapid membrane permeability and efficient nuclear localization, whereas Doxorubicin—despite its smaller molecular weight—exhibits slower and more limited cellular accumulation. Bevilacqua et al. (2019) reported that Doxorubicin enters cells at a significantly reduced rate compared to membrane-permeable nuclear dyes like Hoechst,

which helps explain why Hoechst consistently produces stronger nuclear signals, even at comparable molar concentrations [25].

The transition from cellular to tissue environments imposes additional barriers that further limit Doxorubicin distribution. Khosrawipour et al. (2019) reported that Doxorubicin penetrates tissue to an average depth of only ~252 μm in untreated samples, highlighting its limited ability to diffuse through dense tissue environments [26]. This helps explain the progressive reduction in Doxorubicin signal from ROIs 1–2 to ROIs 3–4, where denser tissue architecture impedes both transport and fluorescence detection. Moreover, microenvironmental factors within tissues can further diminish Doxorubicin's fluorescence. Rastogi et al. (2018) demonstrated that Doxorubicin undergoes significant quenching when bound to specific cellular components or confined within tissue matrices [27]. This environmentally induced quenching compounds the drug's already limited fluorescence efficiency, contributing to its particularly weak signal in tissue-covered ROIs compared to regions with isolated cells or membrane-only baseline measurements. Together, these factors provide a comprehensive explanation for the consistently lower fluorescence intensity of Doxorubicin relative to Hoechst across all ROIs, as well as the pronounced signal reduction observed in tissue-covered regions versus more superficial measurement areas.

5. Discussion

The OSmini platform advances *ex vivo* drug delivery systems by addressing key limitations in earlier microfluidic designs and enabling experiments that model tumor heterogeneity more effectively. Unlike conventional high-throughput screening platforms that prioritize the number of drug conditions tested, OSmini introduces a gradient-based design that shifts the focus toward spatial pharmacodynamics—an underexplored yet critical aspect of drug response. The platform replaces PDMS-based soft lithography with digitally manufactured PMMA, thereby overcoming fabrication barriers and eliminating PDMS's small-molecule absorption, which otherwise alters effective drug concentrations. Flow characterization

confirmed that channel-to-channel variability remained below 8%, establishing a controlled environment for quantitative drug testing. This improvement directly resolves a major limitation of many *ex vivo* systems, where inconsistent fluid delivery can obscure true biological variation.

CNC milling further enhances OSmini's fabrication process compared to traditional microfabrication techniques. With a total build time of approximately 162 minutes, OSmini significantly reduces production timelines relative to the multi-day process required for PDMS-based systems. This speed enables rapid design iteration and lowers the barrier to adoption for labs without specialized microfabrication infrastructure. The optimized chloroform vapor-assisted thermal bonding protocol (4-minute exposure, 140°F, 240 psi for 6 minutes) consistently produced robust sealing across multiple device iterations. This method outperforms traditional liquid solvent bonding by minimizing channel deformation and ensuring strong interfacial adhesion.

Fluorescein-based lateral diffusion studies established key operational parameters that define OSmini's spatial resolution. At flow rates ≥5 mL/hr, fluorescein remained confined to its assigned delivery lanes with minimal lateral spread. However, at flow rates below 2 mL/hr, fluorescence profiles broadened significantly. These flow-dependent diffusion dynamics suggest that experiments requiring strict lane separation should use higher flow rates, while those modeling gradual concentration gradients can benefit from lower rates. This tunable spatial control distinguishes OSmini from fixed-geometry platforms, making it adaptable to diverse experimental goals.

Despite its improvements, OSmini still exhibits limitations. Lateral diffusion between adjacent channels—especially at flow rates below 2 mL/hr—limits spatial resolution for studies that require sharp concentration boundaries. This diffusion occurred asymmetrically, with preferential spread toward the left side of delivery lanes, indicating subtle pressure imbalances in the device that warrant further engineering refinement. Fixed tissue experiments also revealed unanticipated lateral spread of FITC that did not align with

theoretical expectations based on molecular weight, suggesting that tissue-dye interactions significantly influence spatial distribution beyond passive diffusion. Furthermore, fluorescence-based quantification encountered difficulties with compounds such as Doxorubicin. Its low quantum yield and quenching in tissue led to underestimated penetration, making it challenging to visualize gradients accurately. Although the Doxorubicin gradient experiment revealed a detectable difference between 1× and 0.5× concentrations, the fluorescence signal lacked the clear concentration dependence expected—highlighting the challenge of working with poorly fluorescent compounds.

CNC milling improved reproducibility compared to PDMS-based methods, but the observed 8% variability between channels still introduces baseline noise that can obscure subtle drug responses. This variability could particularly affect studies of immune cell chemotaxis or threshold-dependent signaling, where precise dose control is critical. These findings emphasize the need to pair OSmini with complementary analytical tools and define future engineering targets for platform improvement.

Experiments with fluorescent dye delivery in fixed and fresh PY8119 tumor slices validated OSmini's ability to deliver regionally controlled compounds through dense tissue. The spatial distribution of FITC, PI, and Hoechst highlighted how molecular properties influence diffusion. FITC exhibited broad lateral spread, PI showed moderate, time-dependent accumulation, and Hoechst remained tightly confined—consistent with expected molecular transport behavior in heterogeneous tissue. These results support the idea that molecules with strong binding affinity to cellular components maintain sharper spatial gradients and are better suited for spatial pharmacodynamic studies.

The Doxorubicin delivery experiment further demonstrated OSmini's potential for translational applications. While the gradient was difficult to visualize due to weak fluorescence, the platform still enabled spatially controlled delivery of a chemotherapeutic agent—mimicking *in vivo* exposure heterogeneity. Unlike bulk testing methods that average responses across the tissue, OSmini allows researchers to assess region-specific drug

effects and define the minimum concentration required to elicit a therapeutic response in different microenvironments.

Unexpectedly, perfused tissue slices showed signs of cellular migration beyond the original tissue boundaries. This observation suggests that OSmini may support studies of chemotaxis and motility in response to spatial gradients—offering an opportunity to study dynamic behaviors not accessible in dissociated cell systems. Because the platform preserves the architectural and stromal context of the native tumor, it enables investigations into movement-based resistance mechanisms and tumor progression.

Within the landscape of *ex vivo* drug testing, OSmini occupies a unique niche. Organoid models offer high-throughput capacity but lack native tissue architecture. Traditional tumor slice cultures maintain tissue structure but cannot precisely control spatial delivery. OSmini bridges these approaches by combining preserved microenvironmental complexity with controlled, multiplexed drug delivery. Its ability to form concentration gradients aligns with emerging research that shows tumor cells respond differently to steep versus shallow gradients—responses that may underlie adaptive resistance mechanisms [15]. By enabling spatially resolved studies of these phenomena, OSmini contributes to the growing effort to incorporate spatial pharmacology into cancer research.

From a translational standpoint, OSmini offers potential value for personalized medicine. By profiling drug penetration and efficacy in patient-derived tissue slices, the platform can identify compounds that exhibit favorable distribution characteristics within individual tumors. When combined with genomic and phenotypic profiling, these data could inform personalized treatment strategies—particularly for cases where drug penetration poses a barrier to efficacy.

In summary, OSmini represents a significant step forward in tumor slice culture technology. It enables spatially resolved drug delivery, improves fabrication reproducibility, and supports studies of both pharmacodynamic response and dynamic cellular behaviors. Continued development and integration of this platform into preclinical workflows may

improve understanding of tumor biology and support the design of more effective, spatially informed cancer therapies.

6. Conclusion and Future Work

The OSmini platform fills a critical gap in cancer research by enabling spatially controlled, gradient-based drug delivery across intact tumor slices—closely replicating the heterogeneity of *in vivo* tumor microenvironments. Unlike previous microfluidic platforms that prioritize testing the maximum number of drug conditions, OSmini emphasizes the importance of modeling realistic concentration gradients. This work successfully delivered fluorescent dyes and Doxorubicin to both fixed and fresh tumor tissue, establishing a foundation for more physiologically relevant *ex vivo* drug screening. The platform's ability to form gradients aligns with emerging evidence that spatial drug distribution significantly influences treatment efficacy. Tumor cells may respond differently to steep versus shallow gradients—behavior that can drive treatment resistance but often remains undetected in uniform-exposure models [15].

Several future enhancements could improve the OSmini platform's performance and broaden its applications. Technically, refining channel geometry and spacing could improve isolation and reduce lateral diffusion between adjacent lanes. Incorporating additional buffer channels or optimizing flow parameters may further enhance spatial control. Standardizing methods for quantifying three-dimensional drug distribution—potentially through integration with light sheet microscopy or tissue clearing protocols—could provide deeper insights into compound transport. Adding programmable flow control systems would allow real-time adjustments to delivery rates, supporting dynamic gradient studies and time-dependent exposure protocols. Integrating oxygen, pH, or metabolite sensors could offer real-time feedback on tissue viability and metabolic activity during experiments.

Biologically, OSmini could support immune cell migration studies by modeling chemokine gradients that drive immune infiltration at tumor boundaries—critical for evaluating immunotherapy mechanisms. Its multiplexing capabilities could enable spatially controlled

co-delivery of therapeutic agents, helping to uncover synergistic or antagonistic drug interactions across defined regions. Adapting the platform for patient-derived tumor slices would allow researchers to conduct personalized drug response profiling with spatial resolution not achievable through conventional bulk assays. Extending the tissue viability window beyond the current experimental timeframe would also support investigations into delayed drug effects, adaptive resistance, and long-term tissue remodeling.

On the translational front, future development efforts could validate OSmini's predictive accuracy by systematically comparing *ex vivo* drug response data to *in vivo* therapeutic outcomes. Scaling up manufacturing through streamlined production protocols would make the platform accessible to a broader range of research labs and clinical partners. Linking spatial drug delivery with downstream molecular analysis workflows—such as transcriptomics, proteomics, or spatial omics—would deepen its utility for mechanistic studies. Creating user-friendly software tools for experimental setup, flow control, and data visualization would reduce technical barriers and promote adoption across diverse research environments.

By continuing to refine and apply this platform, researchers can expand its impact on the field of tumor biology and drug development. OSmini offers a unique tool for studying how spatial pharmacodynamics influence treatment efficacy and resistance, providing experimental capabilities that extend beyond the limitations of traditional models. As cancer therapies increasingly rely on spatially precise interventions, OSmini stands positioned to contribute meaningfully to both preclinical drug testing and the future of personalized oncology.

7. References

[1] R. L. Siegel, T. B. Kratzer, A. N. Giaquinto, H. Sung, and A. Jemal, "Cancer statistics, 2025," *CA. Cancer J. Clin.*, vol. 75, no. 1, pp. 10–45, Jan. 2025, doi: 10.3322/caac.21871.

[2] A. Honkala, S. V. Malhotra, S. Kummar, and M. R. Junttila, "Harnessing the predictive power of preclinical models for oncology drug development," *Nat. Rev. Drug Discov.*, vol. 21, no. 2, pp. 99–114, Feb. 2022, doi: 10.1038/s41573-021-00301-6.

[3] M. Kapałczyńska *et al.*, "2D and 3D cell cultures – a comparison of different types of cancer cell cultures," *Arch. Med. Sci.*, 2016, doi: 10.5114/aoms.2016.63743.

[4] I. W. Mak, N. Evaniew, and M. Ghert, "Lost in translation: animal models and clinical trials in cancer treatment," *Am. J. Transl. Res.*, vol. 6, no. 2, pp. 114–118, Jan. 2014.

[5] C. H. Wong, K. W. Siah, and A. W. Lo, "Estimation of clinical trial success rates and related parameters," *Biostatistics*, vol. 20, no. 2, pp. 273–286, Apr. 2019, doi: 10.1093/biostatistics/kxx069.

[6] V. Prasad and S. Mailankody, "Research and Development Spending to Bring a Single Cancer Drug to Market and Revenues After Approval," *JAMA Intern. Med.*, vol. 177, no. 11, p. 1569, Nov. 2017, doi: 10.1001/jamainternmed.2017.3601.

[7] A. Letai, P. Bhola, and A. L. Welm, "Functional precision oncology: Testing tumors with drugs to identify vulnerabilities and novel combinations," *Cancer Cell*, vol. 40, no. 1, pp. 26–35, Jan. 2022, doi: 10.1016/j.ccell.2021.12.004.

[8] M. Hidalgo *et al.*, "Patient-Derived Xenograft Models: An Emerging Platform for Translational Cancer Research," *Cancer Discov.*, vol. 4, no. 9, pp. 998–1013, Sep. 2014, doi: 10.1158/2159-8290.CD-14-0001.

[9] R. Sivakumar *et al.*, "Organotypic tumor slice cultures provide a versatile platform for immuno-oncology and drug discovery," *OncoImmunology*, vol. 8, no. 12, p. e1670019, Dec. 2019, doi: 10.1080/2162402X.2019.1670019.

[10] T. C. Chang, A. M. Mikheev, W. Huynh, R. J. Monnat, R. C. Rostomily, and A. Folch, "Parallel microfluidic chemosensitivity testing on individual slice cultures," *Lab Chip*, vol. 14, no. 23, pp. 4540–4551, 2014, doi: 10.1039/C4LC00642A.

[11] A. D. Rodriguez *et al.*, "A microfluidic platform for functional testing of cancer drugs on intact tumor slices," *Lab. Chip*, vol. 20, no. 9, pp. 1658–1675, 2020, doi: 10.1039/C9LC00811J.

[12] L. F. Horowitz *et al.*, "Multiplexed drug testing of tumor slices using a microfluidic platform," *Npj Precis. Oncol.*, vol. 4, no. 1, p. 12, May 2020, doi: 10.1038/s41698-020-0117-y.

[13] H. S. Abyaneh, M. Regenold, T. D. McKee, C. Allen, and M. A. Gauthier, "Towards extracellular matrix normalization for improved treatment of solid tumors," *Theranostics*, vol. 10, no. 4, pp. 1960–1980, 2020, doi: 10.7150/thno.39995.

[14] K. Kohli, V. G. Pillarisetty, and T. S. Kim, "Key chemokines direct migration of immune cells in solid tumors," *Cancer Gene Ther.*, vol. 29, no. 1, pp. 10–21, Jan. 2022, doi: 10.1038/s41417-021-00303-x.

[15] F. Fu, M. A. Nowak, and S. Bonhoeffer, "Spatial Heterogeneity in Drug Concentrations Can Facilitate the Emergence of Resistance to Cancer Therapy," *PLOS Comput. Biol.*, vol. 11, no. 3, p. e1004142, Mar. 2015, doi: 10.1371/journal.pcbi.1004142.

[16] A. Naderi, N. Bhattacharjee, and A. Folch, "Digital Manufacturing for Microfluidics," *Annu. Rev. Biomed. Eng.*, vol. 21, no. 1, pp. 325–364, Jun. 2019, doi: 10.1146/annurev-bioeng-092618-020341.

[17] M. M. Faghih and M. K. Sharp, “Solvent-based bonding of PMMA–PMMA for microfluidic applications,” *Microsyst. Technol.*, vol. 25, no. 9, pp. 3547–3558, Sep. 2019, doi: 10.1007/s00542-018-4266-7.
[18] “f7250pis.pdf.” Accessed: May 07, 2025. [Online]. Available: https://www.sigmaaldrich.com/deepweb/assets/sigmaaldrich/product/documents/222/544/f7250pis.pdf?srsltid=AfmBOopVLY3V1-9flCd5hPXd5UPrOe-by-M6_nVDzIi3BI3SiUuhgwYv
[19] K. A. K. Tanaka *et al.*, “Membrane molecules mobile even after chemical fixation,” *Nat. Methods*, vol. 7, no. 11, pp. 865–866, Nov. 2010, doi: 10.1038/nmeth.f.314.
[20] S. P. Perfetto *et al.*, “Amine reactive dyes: An effective tool to discriminate live and dead cells in polychromatic flow cytometry,” *J. Immunol. Methods*, vol. 313, no. 1–2, pp. 199–208, Jun. 2006, doi: 10.1016/j.jim.2006.04.007.
[21] G. Lukinavičius *et al.*, “SiR–Hoechst is a far-red DNA stain for live-cell nanoscopy,” *Nat. Commun.*, vol. 6, no. 1, p. 8497, Oct. 2015, doi: 10.1038/ncomms9497.
[22] “MAN0011717_Hoechst_33342_UG.pdf.” Accessed: May 07, 2025. [Online]. Available: https://assets.thermofisher.com/TFS-Assets/LSG/manuals/MAN0011717_Hoechst_33342_UG.pdf
[23] PubChem, “Texas Red.” Accessed: May 07, 2025. [Online]. Available: https://pubchem.ncbi.nlm.nih.gov/compound/452705
[24] M. Y. Berezin and S. Achilefu, “Fluorescence Lifetime Measurements and Biological Imaging,” *Chem. Rev.*, vol. 110, no. 5, pp. 2641–2684, May 2010, doi: 10.1021/cr900343z.
[25] P. Mohan and N. Rapoport, “Doxorubicin as a Molecular Nanotheranostic Agent: Effect of Doxorubicin Encapsulation in Micelles or Nanoemulsions on the Ultrasound-Mediated Intracellular Delivery and Nuclear Trafficking,” *Mol. Pharm.*, vol. 7, no. 6, pp. 1959–1973, Dec. 2010, doi: 10.1021/mp100269f.
[26] V. Khosrawipour, S. Reinhard, A. Martino, T. Khosrawipour, M. Arafkas, and A. Mikolajczyk, “Increased Tissue Penetration of Doxorubicin in Pressurized Intraperitoneal Aerosol Chemotherapy (PIPAC) after High-Intensity Ultrasound (HIUS),” *Int. J. Surg. Oncol.*, vol. 2019, pp. 1–6, Dec. 2019, doi: 10.1155/2019/6185313.
[27] T. B. Uyar, K. Wu, M. He, I. Khan, M. Royzen, and M. V. Yigit, “Switchable Fluorescence of Doxorubicin for Label-Free Imaging of Bioorthogonal Drug Release,” *ChemMedChem*, vol. 15, no. 11, pp. 988–994, Jun. 2020, doi: 10.1002/cmdc.202000065.